

1 **Transcriptional activation of cholesterol metabolism in *BRAF^{V600E}*-driven**
2 **serrated colorectal neoplasia.**

3 Paulina Rzasa^{1†}, Sarah Whelan^{1†}, Pooyeh Farahmand^{1†}, Hong Cai¹, Inna Guterman¹,
4 Raquel Palacios-Gallego¹, Shanthi S Undru¹, Lauren Sandford¹, Caleb Green¹, Emma
5 Parrott¹, Hong Jin¹, Fiona Hey¹, Susan Giblett¹, Nicolas B Sylvius², Natalie S Allcock³,
6 Anna Straatman-Iwanowska³, Roberto Feuda⁴, Cristina Tufarelli¹, Karen Brown¹,
7 Catrin Pritchard¹ and Alessandro Rufini^{1,5*}.

8 ¹Leicester Cancer Research Centre, University of Leicester, Leicester, UK.

9 ²NUCLEUS Genomics, Core Biotechnology Services, University of Leicester,
10 Leicester, UK.

11 ³University of Leicester Core Biotechnology Services Electron Microscopy Facility,
12 Leicester, UK.

13 ⁴Department of Genetics and Genome Biology, University of Leicester, Leicester, UK.

14 ⁵Dipartimento di Bioscienze, University of Milan, Milan, Italy.

15 [†]These authors equally contributed to this work.

16 **Running title:** Cholesterol biosynthesis contributes to intestinal hyperplasia in
17 *BRAF^{V600E}* mutant colorectal cancers

18 *Corresponding author:

19 Alessandro Rufini, PhD

20 Dipartimento di Bioscience, Via Celoria 26

21 20133, Milano, MI, Italy

22 **Email:** Alessandro.Rufini@unimi.it

23

24 **Abstract**

25 *BRAF* mutations occur early in serrated colorectal cancers, but their long-term
26 influence on tissue homeostasis are poorly characterized. We investigated the impact
27 of short-term (3 days) and long-term (6 months) expression of *Braf*^{V600E} in the intestinal
28 tissue of an inducible mouse model. We show that *Braf*^{V600E} perturbs the homeostasis
29 of intestinal epithelial cells, with impaired differentiation of enterocytes emerging after
30 prolonged expression of the oncogene. Moreover, *Braf*^{V600E} leads to a persistent
31 transcriptional reprogramming with enrichment of numerous gene signatures
32 indicative of proliferation and tumorigenesis, and signatures suggestive of metabolic
33 rewiring. We focused on the top-ranking cholesterol biosynthesis signature and
34 confirmed its increased expression in human serrated lesions. Functionally, the
35 cholesterol lowering drug atorvastatin prevents the establishment of intestinal crypt
36 hyperplasia in *Braf*^{V600E}-mutant mice. Overall, our work unveils the long-term impact
37 of *Braf*^{V600E} expression in intestinal tissue and suggests that colorectal cancers with
38 mutations in *BRAF* might be prevented by statins.

39 Introduction

40 The single-layered intestinal epithelium contains functionally distinct cellular
41 populations. Proliferating intestinal stem cells (ISCs), whose self-renewal depends on
42 active Wnt/ β -catenin signaling¹, are interspersed among Paneth cells at the bottom of
43 epithelial invaginations, known as crypts of Lieberkühn, and can be identified by
44 selective markers such as LGR5 and OLFM4^{2,3}. ISCs generate transient amplifying
45 (TA) cells, which have limited proliferative capability and migrate upwards towards
46 intestinal villi where they differentiate into the absorptive enterocyte lineage or the
47 secretory lineage, which includes Paneth cells, enteroendocrine cells (EECs) and
48 goblet cells.

49 Colorectal cancer (CRC) is a heterogeneous disease arising from the intestinal
50 epithelium through two main routes^{4,5}. Firstly, tumors originating from tubular, villous
51 or tubulovillous precursor adenomas (ADs) localize to the left colon, are characterized
52 by sustained Wnt/ β -catenin signaling and are thought to develop from ISCs through a
53 bottom-up fashion⁶⁻⁹. Secondly, tumors located in the right colon arise from precursor
54 sessile serrated lesions (SSLs), characterized by a saw-tooth-shaped folding of the
55 dysplastic epithelium, a flat sessile morphology and a mucinous histology¹⁰. This
56 subtype of CRC develops in a top-bottom fashion through transdifferentiation of
57 committed epithelial cells to gastric metaplasia and enrichment in fetal markers^{6,7,11}.
58 The most common driver mutation of SSLs is an activating mutation of the *BRAF*
59 oncogene¹²⁻¹⁴. A valine to glutamate substitution at codon 600 (V600E) generates a
60 constitutive active mutant ($BRAF^{V600E}$) serine-threonine kinase that is responsible for
61 the activation of the downstream MEK/ERK arm of the MAPK pathway¹⁵. Additional
62 molecular features associated with right-sided colonic neoplasia include CpG island
63 methylator phenotype (CIMP), microsatellite instability (MSI) and loss of TGF signaling

64 10-12,14,16. Recently, heterogeneity of *BRAF*-driven CRCs has been uncovered through
65 bulk RNA sequencing and two main *BRAF^{V600E}* CRC subtypes have been identified
66 based on gene expression profile¹⁷. The BM1 subtype displays a gene expression
67 profile enriched in EMT-related processes, *KRAS* signaling and immune response,
68 whereas the BM2 subtype is enriched in cell-cycle and cycle checkpoints-related
69 processes, such as target genes of the E2F transcription factors and genes involved
70 in the G2 to M transition of the cell cycle.

71 *Braf^{V600E}* has been reported to be a poor oncogene when expressed in the
72 mouse intestinal epithelium, whereby few tumors develops after long latency¹⁸⁻²⁰. This
73 prolonged latency agrees with the knowledge that human CRC develops covertly over
74 10-15 years²¹ and indicates that intestinal tissue harbors the oncogenic *BRAF*
75 mutation for a considerable time despite the absence of any clinical manifestation of
76 the disease. Notwithstanding, little is known about the long-term impact of *BRAF^{V600E}*
77 expression on intestinal homeostasis, and the mechanisms that enable *BRAF*-driven
78 CRC development remain incompletely understood. Recently, the limited intestinal
79 tumorigenesis of *Braf^{V600E}* mutant mice has been attributed to an imbalance between
80 stemness and differentiation, whereby expression of *Braf^{V600E}* promotes differentiation
81 of intestinal epithelial cells at the expense of ISCs^{18,22}.

82 The overall aim of the work described here was to attain a deeper
83 understanding of serrated tumorigenesis and ascertain the impact of long-term
84 expression of *Braf^{V600E}*. To this end, we used a mouse model carrying an inducible
85 *Braf^{V600E}* allele²⁰ targeted to the intestinal epithelium, and performed transcriptional
86 profiling over a 6-month time course. Together with dynamic changes in tissue
87 homeostasis, we show that *Braf^{V600E}* orchestrates a rapid and persistent transcriptional
88 reprogramming characterized by the enrichment of numerous gene signatures

89 associated with *Braf*-driven CRC and additional signatures suggestive of metabolic
90 rewiring. In particular, we observed a robust increase in the expression of cholesterol
91 biosynthesis genes. The functional relevance of those adaptations was confirmed by
92 the ability of atorvastatin, a commonly prescribed pharmacological inhibitor of the
93 mevalonate pathway and cholesterol biosynthesis, to prevent the establishment of
94 crypt hyperplasia in *Braf^{V600E}*-mutant mice. Finally, through the analysis of human bulk
95 and single-cell transcriptomic datasets, we confirmed that an increased cholesterol
96 gene signature is a hallmark of serrated CRC.

97 **Results**

98 **Activation of *Braf^{V600E}* in the intestine leads to crypt hyperplasia and persistence** 99 **of crypt-resident ISCs.**

100 Mice carrying an inducible *Braf^{V600E}* knock-in allele were crossed with *Villin-*
101 *Cre^{ER}* mice to generate *VillinCre^{ER/0}/Braf^{V600E-LSL/+}* (BVE) and control *VillinCre^{ER}/Braf^{+/+}*
102 (WT) mice. Intraperitoneal injection of tamoxifen in BVE mice enabled expression of
103 the mutant *Braf^{V600E}* allele. Mutant BVE mice displayed reduced survival (median
104 survival 414 days versus 622 days in WT mice) (Supplemental Figure 1A) and, as
105 previously reported, neoplasia developed after long latency and with limited
106 penetrance (Supplemental Figure 1B and C)¹⁸⁻²⁰. To gain insight into short- and long-
107 term outcomes of oncogene expression, we performed tissue histology (3 days, 6
108 weeks and 6 months after induction of *Braf^{V600E}*) and transcriptomic analysis (3 days
109 and 6 months after induction) of intestinal tissue of BVE and control mice (Figure 1A
110 and Supplemental Figure 2). Analysis of transcriptomic data using GSEA confirmed a
111 robust expression of a MAPK gene signature in mutant mice (Supplemental Figure 3).

112 Firstly, we assessed whether expression of mutant *BRAF* alters homeostasis
113 of the intestinal crypt. Cell count indicated that as early as 3 days post induction,
114 mutant crypts were hyperplastic (Figure 1B). Hyperplasia was linked to increased cell
115 proliferation (Figure 1C) and was persistent, with a significantly increased numbers of
116 cells detected in intestinal crypts of aged mutant mice (Figure 1D). Previous reports
117 have suggested that expression of *Braf*^{V600E} causes TA cell generation and cellular
118 differentiation at the expense of the ISC population^{18,22}. Using the stem cells marker
119 *Olfm4*², we were able to identify a persistent *Olfm4*+ population localized at the bottom
120 of the intestinal crypt in tissue specimens collected 3 days, 6 weeks and 6 months
121 after induction (Figure 1E). Moreover, stem cell marker genes *Lgr5* and *Olfm4* in BVE
122 mice were expressed at levels comparable to those in control mice 6 months after
123 *Braf*^{V600E} expression (Supplemental Figure 4A). We also interrogated transcriptomic
124 data, performing GSEA of an ISC signature. This analysis showed a mild
125 downregulation early after *Braf* activation, but this was reverted in 6 month tissues
126 (Supplemental Figure 4B).

127 However, whereas in WT mice ISCs were interspersed with Paneth cells, in
128 long-term induced mice ISCs clustered at the bottom of the intestinal crypt in long-
129 term induced mice (Figure 1D, insets), following a generalized loss and delocalization
130 of Paneth cells (Supplemental Figure 5). Finally, in keeping with the role of *Braf*^{V600E}
131 in serrated neoplasia, villi from BVE mice developed a saw-toothed appearance early
132 after oncogene expression (Supplemental Figure 6A) and, consistent with the
133 establishment of tissue hyperplasia (see below), villi length was significantly increased
134 in 6 weeks and 6 months mutant mice (Supplemental Figure 6B).

135 **Expression of *Braf*^{V600E} modifies the abundance and distribution of**
136 **differentiated intestinal populations**

137 We then assessed the impact of mutant *Braf* on differentiated intestinal cell
138 populations. As early as 6 weeks post induction of *BRAF^{V600E}*, the intestinal crypts
139 were deprived of Paneth cells, which migrated upwards towards the villi (Supplemental
140 Figures 5) and were progressively lost, a phenotype previously observed in mouse
141 models with altered MAPK activity²³.

142 In addition, GSEA revealed an initial increase in the expression of an intestinal
143 differentiation gene signature 3 days post *Braf^{V600E}* induction. However, unexpectedly,
144 the same signature was downregulated following long-term expression of mutant *Braf*
145 (Figure 2A). At this stage, we also identified a significant downregulation of an
146 intestinal enterocyte signature, which was reflected by reduced Alpl histological
147 staining (Figure 2B and C). A late impairment in the differentiation of enterocytes was
148 confirmed by TEM, which showed shortened and less abundant microvilli on the
149 surface of mutant enterocytes (Figure 2D).

150 Next, we visualized and quantified mucus-producing goblet cells and EECs
151 using Alcian Blue staining and immunofluorescence staining for Chromogranin A
152 (ChrA), respectively (Supplemental Figure 7). Quantification of Alcian Blue- and ChrA-
153 positive cells revealed an increased number of goblet cells, whereas EECs were
154 reduced after long-term (6 months) expression of *Braf^{V600E}* (Figure 2E). rt-qPCR
155 analysis confirmed the reduced expression of ChrA (Figure 2F).

156 These data suggest that *Braf^{V600E}* alters the balance of intestinal secretory and
157 absorptive cell lineages. The analysis of the long term impact of oncogene expression
158 particularly unveiled a significant impact on the numbers of goblet cells and EECs, and
159 a broader downregulation of gene signatures associated with intestinal differentiation
160 and, more specifically, with enterocyte differentiation.

161 Overall, our data confirm previous evidence of reduced stemness and
162 increased differentiation early after induction of *Braf*^{V600E}. They show, in addition, that
163 those changes are transient and that stemness is restored in the intestinal tissue at
164 the expense of differentiation. These findings emphasize the importance of long-term
165 analysis of oncogene expression in the intestinal tissue and they are congruent with
166 recent data suggesting a top-down origin of human serrated neoplasia triggered by
167 dedifferentiation of intestinal cells⁶.

168 ***Braf*^{V600E} expression regulates a transcriptional program linked to CRC**

169 Next, we identified the molecular pathways regulated by *Braf*^{V600E} by
170 interrogating the Molecular Signatures Database (MSigDB)²⁴ (Supplemental Figure 8).
171 Signatures that scored high included pathways associated with cellular proliferation
172 and the BM2 subtype of human CRC, such as Myc, E2F targets and G2/M checkpoint
173 signatures (Figure 3A), which were significantly enriched as early as 3 days post
174 *Braf*^{V600E} induction. The same signatures were confirmed to be enriched in *BRAF*^{V600E}
175 mutant CRCs compared with normal colon tissue from the TCGA dataset⁸
176 (Supplemental Figure 9). We also observed an enrichment of a canonical Wnt pathway
177 signature in the mouse mutant intestinal tissue (Figure 3B), in agreement with previous
178 findings indicating that activation of *Braf*^{V600E} results primarily in intestinal tumors
179 displaying Wnt-pathway activation^{19,20,22}. More tellingly, long-term activation of
180 *Braf*^{V600E} was associated with the expression of a *BRAF*-mutant CRC signatures that
181 predicts poor prognosis in CRC patients²⁵ (Figure 3C).

182 To ascertain whether MAPK activity was necessary for the establishment of the
183 observed transcriptional changes, we treated mice with the MEK inhibitor PD184352
184 (MEKi). Mice received daily treatments with vehicle or MEKi for 3 consecutive days

185 and were then culled for transcriptomic analysis (Supplemental Figure 10A). MEKi
186 administration achieved a marked decrease in phospho-Erk in intestinal tissue, as
187 assessed by Western blot analysis (Supplemental Figure 10B), and a stark repression
188 of the MAPK signature¹⁹ (Supplemental Figure 10C). Notably, pharmacological
189 inhibition of the MAPK pathway reverted the enrichment of some, but not all,
190 signatures. In particular, the Myc signature, the canonical Wnt signature and the
191 Popovici poor-prognosis signature all depended on a functional MAPK pathway
192 (Figure 3D).

193 The origin of *BRAF*^{V600E} CRC remains elusive. Recent evidence suggests that
194 serrated neoplasia arises through an intermediate gastric metaplasia and a reversion
195 to an embryonic cellular stage, sustained by a fetal gene signature^{6,7,11}. Indeed,
196 serrated lesions show enrichment for gene expression associated with metaplasia and
197 fetal genes (Supplemental Figure 11A). In agreement with previous observations¹¹,
198 expression of *Braf*^{V600E} triggers significant and persistent enrichment of the fetal
199 signature in intestinal tissue, which we show to be dependent on MAPK signaling
200 (Supplemental Figure 11B). However, we did not detect significant changes in the
201 metaplasia gene signature⁶, although two genes within the signature, namely
202 Aquaporin 5 (*Aqp5*) and Annexin A10 (*Anxa10*), were consistently upregulated in
203 mutant tissue in a MAPK-dependent fashion (Supplemental Figure 12). Interestingly,
204 *Anxa10* has been previously reported to be a specific marker for human SSL and
205 CRCs of the serrated pathway^{22,26,27}.

206 Overall, these data indicate that activation of *Braf*^{V600E} orchestrates changes in
207 the intestinal transcriptome that reflect the transcriptional reprogramming underlying
208 colorectal carcinogenesis. These changes are durable, persisting for up to 6 months
209 following oncogene expression.

210 ***Braf*^{V600E} expression rewires gene signatures of cholesterol metabolism to drive**
211 **crypt hyperplasia**

212 We noticed that the top scoring gene signature enriched in *BRAF*-mutant mice
213 was a cholesterol signature at both 3 days and 6 months following *Braf*^{V600E} induction
214 (Figure 4A). The robust increase in this signature was also MAPK-dependent (Figure
215 4B). The leading-edge genes responsible for the signature enrichment included
216 several key metabolic enzymes of the mevalonate pathway, such as *Idi1*, *Mvk*, *Fdft1*,
217 *Fdps*, *Sqle*, *Hmgcs1*, *Mvd*, *Hmgcs2*. Increased expression of cholesterol biosynthesis
218 genes was also confirmed by rt-qPCR on RNA extracted from intestinal tissue (Figure
219 4C). Next we confirmed enrichment of the cholesterol biosynthesis signatures in RNA-
220 seq datasets from two independent mouse models of *BRAF*-driven CRC (Figure
221 4D)^{11,18}.

222 Cholesterol biosynthesis contributes to tumorigenesis and can be inhibited
223 using statins, a widely prescribe category of drugs that target the mevalonate pathway
224 rate-limiting enzyme HMG-CoA reductase. Several studies indicate that regular statin
225 use reduces the incidence of several malignancies, including CRC^{28,29}. Hence, we
226 reasoned that cholesterol biosynthesis contributes to the establishment of the durable
227 crypt hyperplasia observed following induction of *Braf*^{V600E} and its inhibition by statins
228 would prevent the formation of hyperplastic crypts. To test this hypothesis, we treated
229 mice with daily doses of atorvastatin starting one week before induction of *Braf*^{V600E}
230 and collected tissue 3 days post tamoxifen administration. Counting of crypt epithelial
231 cells confirmed that statin treatment prevented the establishment of crypt hyperplasia
232 in mutant intestinal tissue (Figure 4E). Mechanistically, atorvastatin did not alter crypt
233 proliferation (Figure 4F), but significantly increased apoptosis assessed through
234 cleaved PARP immunohistochemistry (Figure 4G).

235 Overall, these data indicate that *Braf*^{V600E} elicits a transcriptional
236 reprogramming of cellular metabolism indicative of increased cholesterol biosynthesis,
237 which contributes to the establishment of tissue hyperplasia by increasing survival of
238 crypt cells. The results suggest that statins might prevent colorectal cancer harboring
239 mutant *BRAF*^{V600E}.

240 **Expression of *BRAF*^{V600E} establishes a network of transcription factors that**
241 **mediates the enrichment in the cholesterol biosynthesis gene signature in**
242 **human SSLs**

243 Next, we investigated whether the enrichment of the cholesterol metabolism
244 gene signature induced by *Braf*^{V600E} in the mouse intestine was preserved in human
245 SSLs. To this end, we analyzed three independent datasets of SSLs, which enabled
246 comparison between SSLs, traditional ADs and normal right colon tissue³⁰⁻³². These
247 analyses showed a robust enrichment in the cholesterol biosynthesis signature when
248 SSLs were compared to either normal tissue or ADs (Figure 5A). Notably, no
249 significant enrichment was observed when ADs were compared to normal tissue
250 control, suggesting that the transcriptional rewiring of cholesterol metabolism is
251 specific to SSL (Supplemental Figure 13A). Since bulk transcriptomic data cannot
252 distinguish between the contributions by tumor or non-tumor cells to signatures'
253 enrichment, we ascertained expression of the cholesterol metabolism signature in
254 transformed epithelial cells, by querying a scRNAseq dataset of SSLs and normal
255 tissue (NL)⁶. Clustering of the SSL and NL single cells revealed six canonical cell types
256 and one serrated specific cell (SSC) subtype⁶ (Figure 5C and Supplemental Figure
257 14A). Notably, when the expression of the cholesterol biosynthesis signatures were
258 scored in the cell clusters using the UCell tool³³, SSCs exhibited significantly higher
259 expression of the signature, compared with other cell types (Figure 5D-E). Key

260 metabolic enzymes of the mevalonate pathway were expressed in SSCs, some of
261 them showing a significant enrichment compared to non-cancerous cells
262 (Supplemental Figure 14B).

263 These data indicate that the transcriptional metabolic rewiring of cholesterol
264 metabolism observed in *Braf^{V600E}* mouse intestinal tissue recapitulates comparable
265 adaptations of human colorectal lesions and is a feature of serrated lesions.

266 To investigate how *BRAF^{V600E}* increases transcription of the cholesterol gene
267 signature in human SSLs, we first applied the SCENIC method³⁴ to infer transcription
268 factors and gene regulatory networks from scRNA-seq data of SSLs and NL. By doing
269 so, we identified regulons that are specific to annotated cell types based on RSS³⁵
270 (Supplementary Figure 15). Next, we employed iRegulon³⁶ to pinpoint which
271 transcription factors active in SSCs were predicted to regulate the differentially
272 expressed genes within the cholesterol gene signature (cut off ≥ 5 target genes). We
273 singled out six transcription factors, namely *CEBP*, *CREB3*, *NR2F1*, *KLF16*, *SP6* and
274 *FOSL1*, whose regulons are strongly enriched in SSCs (Figure 6A) and which
275 contribute towards the establishment of the cholesterol metabolism signature in SSCs
276 (Figure 6B).

277 Discussion

278 Ten percent of human CRCs, which originate from serrated lesions, harbor the
279 V600E mutation in the *BRAF* oncogene¹³. This mutation is thought to contribute to
280 tumorigenesis through the activation of the MEK/ERK arm of the MAPK pathway. Yet,
281 despite the development of CRC being a decade long process, the long-term impact
282 of oncogene expression on the intestinal epithelium has not been investigated. Here,
283 for the first time, we assessed this issue using a genetically modified mouse model,

284 the *VillinCre^{ER/0}/Braf^{V600E-LSL/+}* (BVE), which enables tamoxifen-inducible expression of
285 mutant *Braf^{V600E}* in the intestinal epithelium. We used a combination of transcriptomic
286 and histological analyses to compare short-term and long-term impacts of *Braf^{V600E}*
287 expression. By doing so, we were able to identify changes in intestinal epithelial
288 populations that were evident only after prolonged oncogene expression. Interestingly,
289 despite failing to observe any loss of ISCs as reported by others^{18,22}, we did find
290 downregulation of the ISC signature early after *Braf^{V600E}* induction. However, ISC
291 signature was recovered and downregulation reverted after 6 months. Although it is
292 currently unclear what enables this adaptation in the BVE mice, these changes could
293 be explained by the well-established plasticity of the intestinal epithelial cells³⁷. A
294 striking alteration of Paneth cells was evident in 6-week and 6-month induced animals.
295 Paneth cells lost their localization at the base of the intestinal crypt and migrated
296 towards the villi, where they displayed a rounded morphology and were similar to the
297 intermediary cells expressing both Goblet and Paneth cell markers described by
298 Riemer and colleagues²². A similar phenotype was reported in other mouse models
299 with intestinal expression of *Braf^{V600E}* and a MAPK-dependent loss of Paneth cells was
300 also described in models of mutant *Kras*^{18,23,38}. Consistent with these observations,
301 analysis of intestinal tissue after long-term *Braf^{V600E}* activation revealed an impact on
302 other secretory lineages. We observed changes in numbers of both Goblet cells and
303 EECs. However, it should be noted that this reduction does not reflect the total number
304 of cells. Indeed, since villi length was increased in mutant mice, cell numbers were
305 normalized to villi length. Notwithstanding, reduction in RNA levels of *ChrA* confirmed
306 a general reduction in EECs. Whereas the increase in goblet cells probably reflects
307 the mucinous nature of serrated neoplasia, the changes in EECs are particularly
308 intriguing. Indeed, human *BRAF^{V600E}* CRCs accumulate EEC progenitor cells that fail

309 to complete their differentiation. These progenitor EECs secrete the TFF3 protein, a
310 member of the Trefoil family, which supports CRC progression through activation of
311 the PI3K/AKT pathway³⁹. These data warrant additional research into the impact of
312 *BRAF* mutations on the differentiation and activity of EECs in the context of serrated
313 neoplasia.

314 Transcriptomic analysis through GSEA confirmed a negative enrichment of an
315 intestinal differentiation signature after prolonged *Braf*^{V600E} expression. This was likely
316 driven by a significant downregulation of an enterocyte differentiation signature, which,
317 to the best of our knowledge, has not been reported previously. The possible reduction
318 in enterocytes was confirmed by reduced Alpl staining in intestinal tissue. Overall, our
319 data suggest that the long-term impact of *BRAF*^{V600E} is associated with a reduction in
320 tissue differentiation, perhaps necessary to rebalance the initial decrease in
321 stemness^{18,22}. These data are in agreement with published evidence indicating that
322 *BRAF*^{V600E} suppresses hallmarks of intestinal differentiation, which can be restored
323 upon pharmacological inhibition of the MAPK pathway⁴⁰.

324 The activation of *Braf*^{V600E} led to a rapid and persistent enrichment in MAPK-
325 dependent gene signatures associated with proliferation and CRC progression,
326 including a fetal-like gene signature, a Myc signature, a G2/M signature and an E2F
327 target gene signature. The latter two have been described as significant features of
328 the BM2 molecular subtype of CRC¹⁷. We also observed the induction of a Wnt
329 signaling related signature, which was promptly downregulated by inhibition of the
330 MAPK pathway. The association between Wnt pathway and *BRAF*-driven CRC is still
331 unclear. In mice, Rad and colleagues observed a progressive increase in Wnt
332 activation during neoplasia progression¹⁹, which was associated with nonsense or
333 frameshift mutations in the *Apc* gene and activating mutations in the *Ctnnb1* gene,

334 which encodes β -catenin. Mutations affecting Wnt-related genes have also been
335 reported in human serrated CRCs. Truncating mutations of the Wnt negative regulator
336 gene *RNF43* are common in MSI CRCs⁴¹, and non-truncating mutations in the *APC*
337 gene have also been detected⁴². However, the contribution of Wnt signaling to MSI
338 CRCs remains controversial with some studies reporting lack of aberrant nuclear β -
339 catenin localization⁴³, a surrogate marker for Wnt pathway activation, but others
340 showing significant nuclear accumulation in more advanced serrated lesions^{42,44}.
341 Notwithstanding, GSEA in BVE mice indicates that, despite the lack of neoplastic
342 lesions, expression of *Braf*^{V600E} triggers a transcriptional reprogramming congruent
343 with tumorigenesis.

344 Metabolic rewiring is a common hallmark of cancer, including CRC⁴⁵⁻⁴⁷ and we
345 have recently, reported on the role of amino acid metabolism in CRC progression^{48,49}.
346 Here, we provide novel data that strongly support the establishment of a
347 transcriptionally-driven metabolic reprogramming of cholesterol biosynthesis following
348 activation of *Braf*^{V600E}. We have also confirmed similar changes in human datasets of
349 SSLs, suggesting that this metabolic adaptation is a feature of serrated neoplasia.
350 Using bioinformatics tools SCENIC and iRegulon, we have finally identified the chief
351 transcription factors that are responsible for the transcriptional rewiring: *CEBP*,
352 *CREB3*, *NR2F1*, *KLF16*, *SP6* and *FOSL1*. The transcription factor CREB3 has been
353 linked to regulation of cholesterol in response to the unfolded protein response⁵⁰.
354 Similarly, the orphan nuclear receptors NR2F1 and 2 (also known as chicken
355 ovalbumin upstream-promoter transcription factor, COUP-TFI and II) have been
356 reported to regulate genes associated with cholesterol metabolism⁵¹⁻⁵³. A role for
357 FOSL1 in promoting cholangiosarcoma growth through regulation of HMG-CS1 along
358 the mevalonate pathway has also been described⁵⁴. Our data warrant further

359 investigation to dissect the contribution of these transcription factors to the regulation
360 of metabolic rewiring in *BRAF* mutant CRCs and details of their regulation by MAPK.
361 Importantly, statins have been suggested to possess cancer preventive properties, but
362 the association between the occurrence of adenoma or CRC and exposure to statins
363 is controversial^{28,55-57}. Very little is known about whether protection by statins depends
364 on the specific molecular makeup of the tumor⁵⁸. The sensitivity of *BRAF* mutant CRC
365 cell lines to statin treatment has been suggested to depend on BMP signaling through
366 a functional *SMAD4* gene⁵⁹. BMP signaling belongs to the TGF-beta superfamily and
367 mutations in the TGF-beta pathway are common in *BRAF*-mutant CRCs. Whether this
368 affects sensitivity to statins remains to be ascertained. Nonetheless, we observed a
369 similar behavior in the response of *BRAF*-mutant CRC cells to atorvastatin *in vitro*:
370 RKO cells with intact *SMAD4* showed sensitivity to statin treatment, whereas HT29
371 cell harboring homozygous mutations in *SMAD4* were resistant (Supplemental Figure
372 16). These observations are in agreement with the evidence provided here that
373 atorvastatin prevents crypt hyperplasia in the *Braf*-mutant intestine of BVE mice, which
374 harbor a functional BMP pathway.

375 Overall, our data show that one of the most significant and consistent effects of
376 *BRAF^{V600E}* expression in mouse tissue and human serrated lesions is the enrichment
377 of a gene expression signature of cholesterol biosynthesis that contributes to the
378 establishment of epithelial hyperplasia. These findings suggest that the incidence of
379 *BRAF*-mutant CRC could be reduced using statins and warrant further targeted
380 investigations into the specific statin sensitivity of this subtype of CRC.

381 **Materials and Methods**

382 **Cell lines and MTT assay**

383 HT29 CRC cells were grown in DMEM supplemented with 10% foetal calf
384 serum (FCS) and Glutamax. RKO CRC cells were grown in MEM supplemented with
385 10% FCS and Glutamax. Cells were incubated at 37°C and 5% CO₂. For MTT assay,
386 500 to 2000 cells were plated in 96-well plates. A 50 mM atorvastatin in DMSO stock
387 solution was diluted in media (supplemented with dialyzed serum) to concentrations
388 of 1, 5 and 10 µM. Three 96-well plates were run for each assay, each treated for
389 either 24, 48 or 72 hrs. Cells were then incubated with MTT (2.5 mg/ml) at 37°C 2 hrs.
390 To dissolve the formazan produced by the metabolism of MTT, 50 µl of DMSO was
391 added to each well. The plates were then incubated for 30 minutes on a shaker before
392 the optical density was read using a FluoStar OPTIMA plate reader (BMG-Labtech
393 Ltd, UK).

394 **Mouse colony and genotyping**

395 All mice were C57BL6/j background. All animal experiments were performed
396 according to Home Office guidelines under project licenses (PPL) PC4E1710A and
397 P7B8067BB. Mice were housed in the pathogen-free Preclinical Research Facility
398 (PRF) at the University of Leicester and were fed ad libitum with AIN93 diet (TestDiet,
399 USA, Cat#5801-G), under a climate-controlled environment with 12hr day/night cycle.
400 For transgene induction, 8-12 week-old double heterozygous *VillinCre*^{ER/0}/*Braf*<sup>V600E-
401 LSL/+</sup> mice received intraperitoneal injections of 1 mg tamoxifen on five consecutive
402 days at 24hr intervals, unless otherwise stated. Tamoxifen solution was prepared as
403 a 10 mg/ml stock solution solubilized in corn oil. Control mice were *VillinCre*^{ER/0}/*Braf*^{f/+}
404 which received tamoxifen, or *VillinCre*^{ER/0}/*Braf*^{V600E-LSL/+} treated with vehicle. After
405 euthanasia, the small intestine was flushed with PBS and cut into 6 sections rolled to
406 create a “Swiss roll” and fixed in 4% [w/v] paraformaldehyde on a shaker overnight at
407 room temperature. Fixed tissues were placed in embedding cassettes and submerged

408 in 70% ethanol and processed by the Core Biotechnology Services (CBS) histology
409 facility, University of Leicester. Small pieces of tissue (~0.5 cm) were snap frozen in
410 liquid nitrogen for protein extraction or snap frozen in RNAlater solution (Sigma) for
411 RNA extraction.

412 DNA from mouse ear snips was extracted using the DNeasy Blood & Tissue Kit
413 (QIAGEN) according to the manufacturer's instructions. PCR reaction mix for the *Braf*
414 locus was: 10.5 µL of template DNA, OCP 125 (FWD primer) 1 µL (10 pmol), OCP
415 137 (REV-HET primer), 0.5 µL (5 pmol) OCP 143 (REV-WT primer) 0.5µL (5 pmol),
416 MyTaq Red (2x) (Meridian Bioscience BIO-25043) 12.5 µL. The PCR program was:
417 95°C for 2 min, 30 cycles of 94°C for 15 seconds, 60°C for 15 seconds, 72°C for 15
418 seconds; 5 min at 72°C. For *Cre^{ER}* genotyping the PCR mix was: 10.5 µL of template
419 DNA, OCP 361 (FWD primer) 1 µL (10 pmol), OCP 362 (REV primer) 1 µL (10 pmol),
420 MyTaq Red (2x) (Meridian Bioscience BIO-25043) 12.5 µL. The PCR program was:
421 95°C for 4 min, 30 cycles of 94°C for 20 seconds, 57°C for 20 seconds, 72°C for 25
422 seconds; 5 min at 72°C. Primers (Sigma) sequences are listed in Supplemental table
423 1. The PCR products were visualized using 1.8% agarose gel with ethidium bromide
424 (0.5 µg/mL) and imaged using the Syngene G:BOX Chemi XR5. Gels were examined
425 for the presence of PCR bands at 140bp (*Braf^{fl-SL-V600E}* allele) and 466bp (wild-type *Braf*
426 allele) and 300 bp (*Villin-CreERT* allele).

427 **Statin treatment *in vivo***

428 Thirteen-week-old female *VillinCre^{ER/0}/Braf^{V600E-LSL/+}* mice received either 10
429 mg/kg atorvastatin by oral gavage or 5% DMSO/PBS vehicle control daily for 12 days.
430 A 20 mg/mL atorvastatin (Generon) stock in DMSO was freshly diluted to a 1 mg/mL
431 working solution in PBS. Days 1-7 of the study were a daily pre-treatment period of

432 atorvastatin/vehicle. Days 8-10 consisted of both atorvastatin/vehicle gavage and
433 intraperitoneal tamoxifen injection to induce *Braf^{V600E}* expression. On the final day of
434 the study at 3-days post- *Braf^{V600E}* induction, mice received intraperitoneal injections
435 of 200 μ L of 20 mM BrdU solution (Sigma) 3 hrs before tissue harvesting.

436 **Histology**

437 Tissue sections (4 μ m) and H&E staining were performed by the Histology
438 Facility, Core Biotechnological Services, University of Leicester.
439 Immunohistochemistry was performed using the Novolink Polymer Detection Systems
440 kit (Leica Biosystems), according to manufacturer's instructions. SuperFrost Plus™
441 Adhesion slides (Fisher Scientific) containing FFPE tissue sections were incubated at
442 65°C for 30 minutes. Tissues were dewaxed and rehydrated through 3-minute serial
443 immersions in xylene, 99% industrial methylated spirit (IMS), and 95% IMS twice each,
444 followed by 5 minutes in running tap water. Following antigen retrieval (Supplemental
445 Table 2), slides were incubated for 5 minutes in peroxidase block, washed twice in
446 PBS, incubated for 5 minutes in the protein block solution and washed twice in PBS.
447 Tissues were incubated with primary antibodies (Supplemental table 2) (3% BSA/PBS)
448 overnight at 4°C. After incubation, sections were incubated in Polymer solution for 30
449 minutes, washed in PBS, and incubated in DAB solution for 5 minutes. Tissues were
450 counterstained in Mayer's hematoxylin for 5 minutes and subsequently washed in tap
451 water. Tissues were dehydrated through 3-minute serial immersions in 95% IMS twice,
452 99% IMS twice, xylene twice. Slides were then mounted onto glass coverslips using
453 DPX (Sigma Aldrich). Whole slide images were acquired using the Nanozoomer XR
454 digital slide scanner (Hamamatsu Photonics) and visualized using NDP.view2
455 software. For immunofluorescence (IF), antigen-retrieved tissues were blocked in 5%
456 BSA/0.3% Triton X-100 in PBS for 30 minutes, washed with 1% BSA/0.3% Triton X-

457 100 in PBS twice for 10 minutes each and incubated with SP-1 Chromogranin A
458 (ChgA) primary antibody (ImmunoStar) overnight at 4°C. Slides were washed the next
459 day in wash buffer solution twice for 10 minutes each. Alexa Fluor 568 secondary
460 antibody (Invitrogen) was incubated for 1 hr at RT in darkness. Slides were washed
461 and sealed with coverslips using ProLong™ Glass Antifade Mountant containing DAPI
462 (Invitrogen™). IF images were captured using the Vectra® Polaris™ imaging system
463 (Akoya Biosciences), and images were viewed using Phenochart software v1.1.0
464 (Akoya Biosciences).

465 Alcian blue staining for visualization of goblet cells was performed using the
466 Alcian Blue (pH 2.5) Stain Kit (Vector Laboratories). Rehydrated slides were heated
467 at 65°C and incubated in 3% acetic acid solution for 3 minutes, followed by incubation
468 with Alcian Blue solution (pH 2.5) for 30 minutes at RT. Sections were rinsed in 3%
469 acetic acid solution, running tap water and distilled water. Sections were then counter-
470 stained with Enhanced Nuclear Fast Red (Vector Laboratories) for 5 minutes, rinsed
471 in running tap water and distilled water, and dehydrated for mounting.

472 Intestinal alkaline phosphatase staining for detection of enterocytes was
473 performed using Vector Red alkaline phosphatase staining kit (Vector Laboratories).
474 Rehydrated slides were incubated in substrate working solution for 30 minutes and
475 washed in running water for 5 minutes. Tissues were counterstained in Mayer's
476 hematoxylin (Leica Biosystems), dehydrated and mounted in DPX.

477 **Electron Microscopy (EM)**

478 All EM reagents were from Agar Scientific, unless otherwise stated. For
479 Transmission Electron Microscope material was fixed overnight at 4°C in 2.5%
480 glutaraldehyde and 4% paraformaldehyde in 0.1M cacodylate buffer, pH7.2 and

481 washed in 0.1M cacodylate buffer. After the secondary fixation in 1% osmium tetroxide
482 and 1.5% potassium ferricyanide (Merck Life Science) at RT, samples were treated
483 with 1% tannic acid (VWR) dehydrated in ethanol series followed by propylene oxide
484 (Merck Life Science) and embedded in Epon 812 (TAAB Laboratory Equipment Ltd).
485 Samples were sectioned to 70 nm thick using a Reichert Ultracut E ultramicrotome,
486 collected onto copper mesh grids and stained for 5 minutes in lead citrate. Samples
487 were viewed on a JEOL JEM-1400 TEM with an accelerating voltage of 120 kV. Digital
488 images were collected with an EMSIS Xarosa digital camera with Radius software.

489 **Western Blotting**

490 Tissues were homogenized in 400 μ l of ice cold RIPA buffer, containing
491 protease inhibitor cocktail, and phosphatase inhibitor cocktail (Roche). The
492 homogenized solution was kept on ice for 10 minutes with vortexing every minute.
493 Samples were then centrifuged for 10 minutes at 12,000 rpm, at 4°C. Supernatants
494 were collected and protein concentration estimated with Lowry assay. Protein lysates
495 were diluted to 1 mg/ml with SDS loading buffer (0.0625 M Tris-HCl pH 6.8, 2% SDS,
496 0.4 ml of 0.025% Bromophenol blue, 20% glycerol, 5% β -mercaptoethanol) and
497 incubated at 95°C for 10 minutes. 15 μ l of each sample was then run on acrylamide
498 gels (Miniprotean III cell, BioRad) with pre-stained SDS-PAGE protein markers (All
499 Blue Precision Plus Protein Standards, BioRad). Samples were then transferred to
500 nitrocellulose membranes (Syngene) using a semi-dry transfer blot (BioRad) as per
501 manufacturer's instructions. For p-ERK1/2 (Rabbit, Cell Signaling, 9101S),
502 membranes were blocked in 5% BSA (Sigma Aldrich, A3059) in TBST for 90 minutes
503 followed by incubation with primary antibody diluted 1:500 in 5% BSA in TBST
504 overnight at 4°C. For ERK2 (Mouse, Santa Cruz, sc-1647) membranes were blocked
505 in 5% milk in TBST and incubated with the primary antibody diluted 1:1000 in 5% milk

506 in TBST overnight at 4°C. Membranes were washed in TBST, 3 times for 10 min each,
507 and then incubated with secondary antibody (1:5000) at room temperature for 1 hour
508 (anti-Rabbit HRP Sigma A6154, anti-Mouse HRP Sigma A4416) followed by TBST
509 washes 3 times. Bands were visualized using SuperSignal West Pico
510 Chemiluminescent substrate kit (Thermo Fisher Scientific, 34580) and photographic
511 film (Fuji).

512 **RNA extraction**

513 RNA was extracted from intestinal tissue on a Promega Maxwell 16 using the
514 Maxwell 16 LEV simplyRNA Cells Kit (Reference AS1270). RNA quality and quantity
515 was assessed using the 2100 Bioanalyzer Instrument (Agilent).

516 **Transcriptomic analysis**

517 *RNA-sequencing (RNA-seq).* For RNA-seq, four *VillinCre^{ER/0}/Braf^{V600E-LSL/+}* 8-
518 12-week old mice were induced with tamoxifen and four were treated with vehicle to
519 be left uninduced and used as controls to identify differentially expressed (DE)
520 genes. Each experimental group contained two male and two female animals. Mice
521 received intraperitoneal injections of 2 mg tamoxifen on two consecutive days.
522 Intestinal tissue was harvested 6 months post-induction. Indexed RNA libraries were
523 prepared using the NEBNext® Single Cell/Low Input RNA Library Prep Kit for
524 Illumina (NEB ref # E6420S) according to manufacturer's standard protocol and
525 sequenced by 75 bp-paired-end sequencing on Illumina Novaseq, with the aim to
526 obtain approximately 25 million reads per sample.

527 *Microarrays.* For microarrays, 12 mice 8-12-week old were split into two groups
528 of six with an equal number of males and females. Six mice were *VillinCre^{ER/0}* controls
529 and six were *VillinCre^{ER/0}/Braf^{V600E-LSL/+}*. Both groups received three consecutive daily

530 doses of 2 mg tamoxifen and tissue was harvested 3 days after the last injection for
531 short term study and 6 months after for the long-term study. Animals subjected to
532 inhibition of MEK kinase with PD184352 treatment received two injections of 100 μ l
533 tamoxifen (10mg/ml) on two consecutive days followed by 3 injections of
534 inhibitor/vehicle on three consecutive days. PD184352 (Selleckchem) was prepared
535 in 10% DMSO (Sigma), 10% Cremophor EL (Calbiochem) in water. RNA was
536 extracted as described above and transcriptome profiling was conducted using the
537 SurePrint G3 Mouse Gene Expression v2 8x60K Microarray Kit (Agilent, #G4852B),
538 according to manufacturer's instructions.

539 **Real-time PCR (rt-qPCR)**

540 Reverse transcription of RNA was performed using the High-Capacity RNA-to-
541 cDNA™ Kit (Applied Biosystems™) with a random primer approach. The 2X master
542 mix was prepared according to the manufacturer's instructions, and 2 μ g of purified
543 RNA was added per 20 μ L reaction. Reactions with and without the reverse
544 transcriptase enzyme were performed in tandem, and samples without the enzyme
545 were used as negative controls in subsequent rt-qPCR assays. The reverse
546 transcription reactions was performed using the program: 25°C for 10 min, 37°C for
547 120 min, 85°C for 5 min.

548 TaqMan® Gene Expression Assays (Fisher Scientific) were used for rt-qPCR
549 reactions (Supplemental Table 3), using the StepOnePlus™ rt-qPCR System (Fisher
550 Scientific) equipped with StepOnePlus™ Software v2.3. The thermocycler program
551 was: 50°C for 2 min, 95°C for 20 sec, then 40 cycles of: 95°C for 1 sec, 60°C for 20
552 sec. Each PCR reaction contained 1 μ L of template DNA/control/water, 5 μ L of 2X
553 TaqMan Fast Advanced Master Mix (Applied Biosystems) and a TaqMan Gene

554 Expression Assay (Thermo Scientific) containing 900 nM forward and reverse primers
555 and 250 nM probe and 10 μ L with nuclease-free water. Each sample was run in
556 technical triplicates. rt-qPCR data were then analyzed using the $\Delta\Delta$ Ct method. Ct
557 values were normalized to endogenous control (EC) genes. We employed the
558 NormFinder Excel Add-In, v0.953⁶⁰ to assess four candidate genes for use as
559 endogenous controls: glucuronidase beta (*Gusb*), beta-2-microglobulin (*B2m*), beta-
560 actin (*Actb*), and TATA-box binding protein (*Tbp*). The top three genes *Gusb*, *B2m*,
561 *Tbp*) with the most stable expression across experimental groups were selected as
562 EC genes for normalization of RT-qPCR assays in accordance with the MIQE
563 guidelines⁶¹.

564 **Bioinformatics analysis**

565 Bioinformatics analysis was performed using the statistical computing software
566 R version 4.0.5 and the integrated development environment program RStudio version
567 1.3.1093. For RNA sequencing, FASTQ files sequencing quality was assessed using
568 FastQC (v0.11.9). Sequencing adapter content was trimmed using FastP (v0.20.0)⁶².
569 The pre-processed reads were then aligned to the mouse GRCm38/mm10 reference
570 genome using Spliced Transcripts Alignment to a Reference (STAR) (v2.7.3a)⁶³. Gene
571 mapping and quantification was performed using DESeq2 (v1.34.0)⁶⁴. For microarray
572 data, the R Bioconductor package Linear Models for Microarray Data (Limma)
573 (v3.50.1) was used to read raw text files from single-channel Agilent RNA microarrays
574 and perform differential expression analysis.

575 **Gene Set Enrichment Analysis (GSEA)**

576 Agilent gene identifiers (IDs) from microarray analysis and RefSeq gene IDs
577 from RNA sequencing were converted into Entrez IDs using BioMart (v2.50.3)⁶⁵ to

578 ensure gene IDs were compatible with GSEA functions and The DE genes were
579 ranked using Wald statistic. The R Bioconductor package clusterProfiler⁶⁶ was used
580 to perform GSEA and statistical testing using Hallmark gene signatures from the
581 Molecular Signatures Database (MSigDB)⁶⁷. P-values were adjusted for multiple-
582 hypothesis testing using the Benjamini-Hochberg method. Enrichment plots were
583 generated using R Bioconductor package enrich plot (v1.14.2).

584 **Analysis of publicly available datasets**

585 Publicly available datasets (GSE106330¹⁸, GSE168478¹¹, E-MTAB-6951³²,
586 GSE45270³⁰ and TCGA-COAD/READ⁸), were obtained from Gene Expression
587 Omnibus (GEO) (<https://www.ncbi.nlm.nih.gov/geo/>), ArrayExpress
588 (<https://www.ebi.ac.uk/arrayexpress/>) and The Cancer Genome Atlas (TCGA)
589 (<https://www.cancer.gov/tcga>). For GSE106330, normalized gene expression matrix
590 was retrieved from GEO. For GSE168478, matrix of raw counts was obtained and
591 further normalized using DESeq2 (v1.36.0) R package. Fastq files were downloaded
592 from ArrayExpress for E-MTAB-6951. Reads, after quality control with fastQC
593 (v0.11.5), were aligned to the human reference genome GRCh38 and quantified using
594 STAR (v2.7.9a) with the following parameters: --quantMode GeneCounts, --
595 outFilterScoreMinOverLread 0.33, --outFilterMatchNmin 40, --
596 outFilterMatchNminOverLread 0.33. Count files were loaded into R and normalized
597 using Deseq2 package. Expression CEL files were downloaded from GSE45270 and
598 loaded into R using read.celfiles() function from affy R package (v1.74.0)⁶⁸.
599 Background correction normalization and expression estimation was done with rma()
600 function. TCGA-COAD/READ STAR count matrices were accessed using
601 TCGAbiolinks R package (v2.24.3)⁶⁹ and normalized with DESeq2 package.

602 GSEA of analyzed public datasets was performed with GSEA software
603 (v4.2.2)⁷⁰. All matrixes, generated as described above, were saved in GCT format.
604 The categorical class file format (cls) was created for each dataset to define phenotype
605 labels. GSEA was performed using default settings except for “Permutation type” set
606 to “gene_set”.

607 **Single-cell RNA sequencing (scRNA-seq) data analysis**

608 *scRNA-seq, data subset and integration*. Publicly available, scRNA-seq QC-
609 filtered (Level 4) discovery (DIS) and validation (VAL) epithelial datasets were
610 downloaded from HTAN data portal: <https://data.humantumoratlas.org/> (HTAN
611 Vanderbilt)⁶. To subset cells of interest, datasets were loaded into Python (v3.9.1) as
612 AnnData objects (v0.7.6)⁷¹. Both datasets contained metadata attributes, such as
613 polyp type and assigned cell type. This information was used to subset cells annotated
614 as SSL (sessile serrated lesion) and NL (normal colonic biopsy) with the *isin* function
615 of the pandas (v1.3.1) package (Reback et al., 2021). In total, 64,382 NL (VAL: 34,008,
616 DIS: 30,374) and 12,986 SSL (VAL: 6,892, DIS: 6,094) cells were subsetted for
617 downstream analysis. Subsets of cells were loaded into R (v3.6.1) to perform
618 integration with Seurat (v3.2.3) R package (Stuart et al., 2019). Prior to integration,
619 datasets were independently log-normalized with the *NormalisationData* function.
620 2,000 features being highly variable for each dataset and across datasets were
621 identified using *FindVariableFeatures* and *SelectingIntegrationFeatures* functions,
622 respectively. A *FindIntegrationAnchors* function with default settings was implemented
623 to perform the unsupervised identification of cells that were used to integrate DIS and
624 VAL datasets together by applying *IntegrateData* function. Further bioinformatics
625 analysis was performed in Seurat (v4.1.1)⁷².

626 *scRNA-seq, dimensional reduction and clustering.* Principal component
627 analysis (PCA) was performed on normalized and scaled data by implementing
628 *RunPCA* function with a features argument set to use variable features. The first 10
629 dimensions of the PCA were used to calculate the neighbors with *FindNeighbors*
630 function. Finally, the graph was segmented into clusters using *FindCluster* function
631 with a resolution adjusted to 0.5. Uniform Manifold Approximation and Projection
632 (UMAP), a non-linear dimensional reduction method, was selected to explore an
633 integrated dataset by implementing *RunUMAP* function with a number of dimensions
634 specified as 10. *DimPlot* function was further used to visualize cells in a low
635 dimensional UMAP space.

636 *scRNA-seq, cell type annotation.* The original cell type annotation, which was
637 included in the metadata, was projected in the UMAP space with *DimPlot* function and
638 used to rename 39 identified clusters by implementing *RenameIdents* function. In total,
639 8 cell types were found within an analyzed subset of SSL and NL cells.

640 *scRNA-seq, gene signature scores, UCell.* UCell (v1.3.1) R package³³ was
641 applied to evaluate cholesterol homeostasis signature distribution in SSL and NL
642 dataset. UCell calculates the gene signature score in individual cells based on the
643 Mann-Whitney U statistic. List of genes involved in cholesterol homeostasis were
644 retrieved from MsigDB⁶⁷. UCell score for cholesterol signature was calculated by
645 implementing *AddModuleScore_UCell* function on Seurat object. Obtained UCell
646 score distribution for SSL and NL dataset was visualized in UMAP space by
647 implementing *FeaturePlot* function. Additionally, a violin plot was generated with
648 *VlnPlot* function to compare cholesterol signature distribution in different cell
649 populations. For statistical analysis, mean comparison p-values were added to violin
650 plots with *stat_compare_means* function from ggpubr (v0.4.0) R package

651 (Kassambara, 2020). Means were compared using the non-parametric Wilcoxon
652 rank sum test with SSC cluster as a reference group.

653 *scRNA-seq, differential expression testing.* The differential testing of
654 expression of cholesterol biosynthesis genes between SSC and remaining cell
655 populations was performed in Seurat. *FindMarkers* function was run with the 'ident.1'
656 argument defining SSC and 'feature' argument specifying a list of cholesterol genes
657 (74 genes) to test. As a result, 21 genes of cholesterol signature were identified as up-
658 (17 genes) and downregulated (4 genes) in SSC population. Additionally, the average
659 expression of genes upregulated in SSC was visualized across all cell types with
660 *DotPlot* function.

661 *scRNA-seq, gene regulatory network.* Single-Cell rEgulatory Network
662 Inference and Clustering (SCENIC) method was applied to infer gene regulatory
663 network in different cell types of SSL and NL dataset. The required input files included
664 scRNAseq expression matrix, which was generated from Seurat object using
665 *build_loom* function of *ScopeLoomR* R package. List of human TFs (1839 genes) and
666 three hg19 gene-motifs ranking databases comparing 10 species in .feather format
667 were downloaded from <https://resources.aertslab.org/cistarget/>. First, the candidate
668 regulatory modules of TFs and target genes were inferred by using the GRNBoost2
669 method (arboreto, v0.1.6). Next, RcisTarget was implemented to remove indirect
670 targets from these modules based on motif discovery. Finally, the activity of predicted
671 regulons was quantified at the cellular resolution by implementing the AUCell
672 algorithm. Further, resulting regulon activity enrichment matrix was jointly analyzed
673 with count-based matrix by using Scanpy (v1.9.1) python package⁷¹. To identify
674 regulons that are specific to the SSC cluster we computed the regulon specificity score
675 (RSS)³⁵. The RSS was calculated for each cell type with *regulon_specificity_scores*

676 function of pySCENIC and the top 30 regulons for each cell type were shown on plot.
677 Regulon activity of selected regulons was visualized on UMAP transcriptomic space
678 with *sc.pl.umap* function of scanpy package.

679 *scRNAse, regulation detection of deregulated cholesterol genes.* A Seurat's
680 table of twenty-one deregulated cholesterol genes in SSC was imported to Cytoscape
681 (v 3.9.1)⁷³, where iRegulon (v1.3)³⁶ was run with default settings to predict TFs
682 potentially regulating the expression of these genes. TFs that were shown previously
683 to be specific for SSC were selected from the combination of motifs and tracks output
684 (cut off > 5 target genes). Generated regulatory network was visualized in Cytoscape
685 with target genes node colored by avg_log2FC.

686 **Statistical analysis**

687 Statistical significance testing was performed using GraphPad Prism 7
688 software. Comparisons between two groups were performed using the two-tailed,
689 unpaired Student's t-test. Comparisons between more than two groups were
690 performed using ANOVA with appropriate post-hoc analysis for multiple comparison
691 (Tukey, Dunnet). Distribution data for intestinal crypts were analyzed using the
692 Kolmogorov-Smirnov test.

693

694

- 695 1 Santos, A. J. M., Lo, Y. H., Mah, A. T. & Kuo, C. J. The Intestinal Stem Cell
696 Niche: Homeostasis and Adaptations. *Trends in cell biology* **28**, 1062-1078,
697 doi:10.1016/j.tcb.2018.08.001 (2018).
- 698 2 van der Flier, L. G., Haegebarth, A., Stange, D. E., van de Wetering, M. &
699 Clevers, H. OLFM4 is a robust marker for stem cells in human intestine and
700 marks a subset of colorectal cancer cells. *Gastroenterology* **137**, 15-17,
701 doi:10.1053/j.gastro.2009.05.035 (2009).
- 702 3 Barker, N. *et al.* Identification of stem cells in small intestine and colon by
703 marker gene Lgr5. *Nature* **449**, 1003-1007, doi:10.1038/nature06196 (2007).
- 704 4 Minoo, P., Zlobec, I., Peterson, M., Terracciano, L. & Lugli, A. Characterization
705 of rectal, proximal and distal colon cancers based on clinicopathological,
706 molecular and protein profiles. *International journal of oncology* **37**, 707-718,
707 doi:10.3892/ijo_00000720 (2010).
- 708 5 Stintzing, S., Tejpar, S., Gibbs, P., Thiebach, L. & Lenz, H. J. Understanding
709 the role of primary tumour localisation in colorectal cancer treatment and
710 outcomes. *European journal of cancer (Oxford, England : 1990)* **84**, 69-80,
711 doi:10.1016/j.ejca.2017.07.016 (2017).
- 712 6 Chen, B. *et al.* Differential pre-malignant programs and microenvironment chart
713 distinct paths to malignancy in human colorectal polyps. *Cell* **184**, 6262-
714 6280.e6226, doi:10.1016/j.cell.2021.11.031 (2021).
- 715 7 Joanito, I. *et al.* Single-cell and bulk transcriptome sequencing identifies two
716 epithelial tumor cell states and refines the consensus molecular classification
717 of colorectal cancer. *Nature genetics*, doi:10.1038/s41588-022-01100-4 (2022).
- 718 8 Muzny, D. M. *et al.* Comprehensive molecular characterization of human colon
719 and rectal cancer. *Nature* **487**, 330-337, doi:10.1038/nature11252 (2012).
- 720 9 Fearon, E. R. & Vogelstein, B. A genetic model for colorectal tumorigenesis.
721 *Cell* **61**, 759-767, doi:10.1016/0092-8674(90)90186-i (1990).
- 722 10 Missiaglia, E. *et al.* Distal and proximal colon cancers differ in terms of
723 molecular, pathological, and clinical features. *Annals of oncology : official
724 journal of the European Society for Medical Oncology* **25**, 1995-2001,
725 doi:10.1093/annonc/mdu275 (2014).
- 726 11 Leach, J. D. G. *et al.* Oncogenic BRAF, unrestrained by TGF β -receptor
727 signalling, drives right-sided colonic tumorigenesis. *Nature Communications*
728 **12**, 3464, doi:10.1038/s41467-021-23717-5 (2021).
- 729 12 Weisenberger, D. J. *et al.* CpG island methylator phenotype underlies sporadic
730 microsatellite instability and is tightly associated with BRAF mutation in
731 colorectal cancer. *Nature genetics* **38**, 787-793, doi:10.1038/ng1834 (2006).
- 732 13 Davies, H. *et al.* Mutations of the BRAF gene in human cancer. *Nature* **417**,
733 949-954, doi:10.1038/nature00766 (2002).
- 734 14 Rajagopalan, H. *et al.* RAF/RAS oncogenes and mismatch-repair status.
735 *Nature* **418**, 934-934, doi:10.1038/418934a (2002).
- 736 15 Dhillon, A. S., Hagan, S., Rath, O. & Kolch, W. MAP kinase signalling pathways
737 in cancer. *Oncogene* **26**, 3279-3290, doi:10.1038/sj.onc.1210421 (2007).
- 738 16 Parsons, R. *et al.* Microsatellite instability and mutations of the transforming
739 growth factor beta type II receptor gene in colorectal cancer. *Cancer research*
740 **55**, 5548-5550 (1995).

- 741 17 Barras, D. *et al.* BRAF V600E Mutant Colorectal Cancer Subtypes Based on
742 Gene Expression. *Clinical cancer research : an official journal of the American*
743 *Association for Cancer Research* **23**, 104-115, doi:10.1158/1078-0432.Ccr-16-
744 0140 (2017).
- 745 18 Tong, K. *et al.* Degree of Tissue Differentiation Dictates Susceptibility to BRAF-
746 Driven Colorectal Cancer. *Cell Reports* **21**, 3833-3845,
747 doi:<https://doi.org/10.1016/j.celrep.2017.11.104> (2017).
- 748 19 Rad, R. *et al.* A genetic progression model of Braf(V600E)-induced intestinal
749 tumorigenesis reveals targets for therapeutic intervention. *Cancer cell* **24**, 15-
750 29, doi:10.1016/j.ccr.2013.05.014 (2013).
- 751 20 Carragher, L. A. *et al.* V600EBraf induces gastrointestinal crypt senescence
752 and promotes tumour progression through enhanced CpG methylation of
753 p16INK4a. *EMBO molecular medicine* **2**, 458-471,
754 doi:10.1002/emmm.201000099 (2010).
- 755 21 Jänne, P. A. & Mayer, R. J. Chemoprevention of colorectal cancer. *The New*
756 *England journal of medicine* **342**, 1960-1968,
757 doi:10.1056/nejm200006293422606 (2000).
- 758 22 Riemer, P. *et al.* Transgenic expression of oncogenic BRAF induces loss of
759 stem cells in the mouse intestine, which is antagonized by β -catenin activity.
760 *Oncogene* **34**, 3164-3175, doi:10.1038/onc.2014.247 (2015).
- 761 23 Feng, Y. *et al.* Mutant KRAS promotes hyperplasia and alters differentiation in
762 the colon epithelium but does not expand the presumptive stem cell pool.
763 *Gastroenterology* **141**, 1003-1013.e1010, doi:10.1053/j.gastro.2011.05.007
764 (2011).
- 765 24 Liberzon, A. *et al.* Molecular signatures database (MSigDB) 3.0. *Bioinformatics*
766 **27**, 1739-1740, doi:10.1093/bioinformatics/btr260 (2011).
- 767 25 Popovici, V. *et al.* Identification of a poor-prognosis BRAF-mutant-like
768 population of patients with colon cancer. *Journal of clinical oncology : official*
769 *journal of the American Society of Clinical Oncology* **30**, 1288-1295,
770 doi:10.1200/jco.2011.39.5814 (2012).
- 771 26 Tsai, J.-H. *et al.* Aberrant expression of annexin A10 is closely related to gastric
772 phenotype in serrated pathway to colorectal carcinoma. *Modern Pathology* **28**,
773 268-278, doi:10.1038/modpathol.2014.96 (2015).
- 774 27 Gonzalo, D. H. *et al.* Gene expression profiling of serrated polyps identifies
775 annexin A10 as a marker of a sessile serrated adenoma/polyp. *The Journal of*
776 *pathology* **230**, 420-429, doi:10.1002/path.4200 (2013).
- 777 28 Lytras, T., Nikolopoulos, G. & Bonovas, S. Statins and the risk of colorectal
778 cancer: an updated systematic review and meta-analysis of 40 studies. *World*
779 *J Gastroenterol* **20**, 1858-1870, doi:10.3748/wjg.v20.i7.1858 (2014).
- 780 29 Mullen, P. J., Yu, R., Longo, J., Archer, M. C. & Penn, L. Z. The interplay
781 between cell signalling and the mevalonate pathway in cancer. *Nature Reviews*
782 *Cancer* **16**, 718-731, doi:10.1038/nrc.2016.76 (2016).
- 783 30 De Sousa, E. M. F. *et al.* Poor-prognosis colon cancer is defined by a
784 molecularly distinct subtype and develops from serrated precursor lesions.
785 *Nature medicine* **19**, 614-618, doi:10.1038/nm.3174 (2013).
- 786 31 Delker, D. A. *et al.* RNA sequencing of sessile serrated colon polyps identifies
787 differentially expressed genes and immunohistochemical markers. *PloS one* **9**,
788 e88367, doi:10.1371/journal.pone.0088367 (2014).

- 789 32 Parker, H. R. *et al.* The proto CpG island methylator phenotype of sessile
790 serrated adenomas/polyps. *Epigenetics* **13**, 1088-1105,
791 doi:10.1080/15592294.2018.1543504 (2018).
- 792 33 Andreatta, M. & Carmona, S. J. UCell: Robust and scalable single-cell gene
793 signature scoring. *Computational and Structural Biotechnology Journal* **19**,
794 3796-3798, doi:<https://doi.org/10.1016/j.csbj.2021.06.043> (2021).
- 795 34 Aibar, S. *et al.* SCENIC: single-cell regulatory network inference and clustering.
796 *Nat Methods* **14**, 1083-1086, doi:10.1038/nmeth.4463 (2017).
- 797 35 Suo, S. *et al.* Revealing the Critical Regulators of Cell Identity in the Mouse Cell
798 Atlas. *Cell Rep* **25**, 1436-1445.e1433, doi:10.1016/j.celrep.2018.10.045 (2018).
- 799 36 Janky, R. *et al.* iRegulon: from a gene list to a gene regulatory network using
800 large motif and track collections. *PLoS Comput Biol* **10**, e1003731,
801 doi:10.1371/journal.pcbi.1003731 (2014).
- 802 37 Beumer, J. & Clevers, H. Regulation and plasticity of intestinal stem cells during
803 homeostasis and regeneration. *Development (Cambridge, England)* **143**, 3639-
804 3649, doi:10.1242/dev.133132 (2016).
- 805 38 de Jong, P. R. *et al.* ERK5 signalling rescues intestinal epithelial turnover and
806 tumour cell proliferation upon ERK1/2 abrogation. *Nat Commun* **7**, 11551,
807 doi:10.1038/ncomms11551 (2016).
- 808 39 Miller, S. A. *et al.* LSD1 and Aberrant DNA Methylation Mediate Persistence of
809 Enteroendocrine Progenitors That Support BRAF-Mutant Colorectal Cancer.
810 *Cancer research* **81**, 3791-3805, doi:10.1158/0008-5472.Can-20-3562 (2021).
- 811 40 Herr, R. *et al.* B-Raf inhibitors induce epithelial differentiation in BRAF-mutant
812 colorectal cancer cells. *Cancer research* **75**, 216-229, doi:10.1158/0008-
813 5472.Can-13-3686 (2015).
- 814 41 Giannakis, M. *et al.* RNF43 is frequently mutated in colorectal and endometrial
815 cancers. *Nature genetics* **46**, 1264-1266, doi:10.1038/ng.3127 (2014).
- 816 42 Borowsky, J. *et al.* The role of APC in WNT pathway activation in serrated
817 neoplasia. *Modern pathology : an official journal of the United States and*
818 *Canadian Academy of Pathology, Inc* **31**, 495-504,
819 doi:10.1038/modpathol.2017.150 (2018).
- 820 43 Panarelli, N. C., Vaughn, C. P., Samowitz, W. S. & Yantiss, R. K. Sporadic
821 microsatellite instability-high colon cancers rarely display immunohistochemical
822 evidence of Wnt signaling activation. *The American journal of surgical*
823 *pathology* **39**, 313-317, doi:10.1097/pas.0000000000000380 (2015).
- 824 44 Yachida, S., Mudali, S., Martin, S. A., Montgomery, E. A. & Iacobuzio-Donahue,
825 C. A. Beta-catenin nuclear labeling is a common feature of sessile serrated
826 adenomas and correlates with early neoplastic progression after BRAF
827 activation. *The American journal of surgical pathology* **33**, 1823-1832,
828 doi:10.1097/PAS.0b013e3181b6da19 (2009).
- 829 45 Cairns, R. A., Harris, I. S. & Mak, T. W. Regulation of cancer cell metabolism.
830 *Nat Rev Cancer* **11**, 85-95, doi:10.1038/nrc2981 (2011).
- 831 46 Vander Heiden, M. G. *et al.* Metabolic pathway alterations that support cell
832 proliferation. *Cold Spring Harb Symp Quant Biol* **76**, 325-334,
833 doi:10.1101/sqb.2012.76.010900 (2011).
- 834 47 Satoh, K. *et al.* Global metabolic reprogramming of colorectal cancer occurs at
835 adenoma stage and is induced by MYC. *Proceedings of the National Academy*
836 *of Sciences of the United States of America* **114**, E7697-e7706,
837 doi:10.1073/pnas.1710366114 (2017).

- 838 48 Alaqbi, S. S. *et al.* Increased mitochondrial proline metabolism sustains
839 proliferation and survival of colorectal cancer cells. *PLoS one* **17**, e0262364,
840 doi:10.1371/journal.pone.0262364 (2022).
- 841 49 Alexandrou, C. *et al.* Sensitivity of Colorectal Cancer to Arginine Deprivation
842 Therapy is Shaped by Differential Expression of Urea Cycle Enzymes. *Sci Rep*
843 **8**, 12096, doi:10.1038/s41598-018-30591-7 (2018).
- 844 50 Ying, Z. *et al.* The Unfolded Protein Response and Cholesterol Biosynthesis
845 Link Luman/CREB3 to Regenerative Axon Growth in Sensory Neurons. *J*
846 *Neurosci* **35**, 14557-14570, doi:10.1523/jneurosci.0012-15.2015 (2015).
- 847 51 Myers, S. A., Wang, S. C. & Muscat, G. E. The chicken ovalbumin upstream
848 promoter-transcription factors modulate genes and pathways involved in
849 skeletal muscle cell metabolism. *J Biol Chem* **281**, 24149-24160,
850 doi:10.1074/jbc.M601941200 (2006).
- 851 52 Rodríguez, J. C., Ortiz, J. A., Hegardt, F. G. & Haro, D. Chicken ovalbumin
852 upstream-promoter transcription factor (COUP-TF) could act as a
853 transcriptional activator or repressor of the mitochondrial 3-hydroxy-3-
854 methylglutaryl-CoA synthase gene. *Biochem J* **326** (Pt 2), 587-592,
855 doi:10.1042/bj3260587 (1997).
- 856 53 Yamazaki, T. *et al.* The COUP-TFII variant lacking a DNA-binding domain
857 inhibits the activation of the Cyp7a1 promoter through physical interaction with
858 COUP-TFII. *Biochem J* **452**, 345-357, doi:10.1042/bj20121200 (2013).
- 859 54 Vallejo, A. *et al.* FOSL1 promotes cholangiocarcinoma via transcriptional
860 effectors that could be therapeutically targeted. *Journal of Hepatology* **75**, 363-
861 376, doi:<https://doi.org/10.1016/j.jhep.2021.03.028> (2021).
- 862 55 Bardou, M., Barkun, A. & Martel, M. Effect of statin therapy on colorectal
863 cancer. *Gut* **59**, 1572, doi:10.1136/gut.2009.190900 (2010).
- 864 56 Jung, Y. S., Park, C. H., Eun, C. S., Park, D. I. & Han, D. S. Statin use and the
865 risk of colorectal adenoma: A meta-analysis. *Journal of gastroenterology and*
866 *hepatology* **31**, 1823-1830, doi:10.1111/jgh.13393 (2016).
- 867 57 Wei, J. T., Mott, L. A., Baron, J. A. & Sandler, R. S. Reported use of 3-hydroxy-
868 3-methylglutaryl coenzyme A reductase inhibitors was not associated with
869 reduced recurrence of colorectal adenomas. *Cancer epidemiology, biomarkers*
870 *& prevention : a publication of the American Association for Cancer Research,*
871 *cosponsored by the American Society of Preventive Oncology* **14**, 1026-1027,
872 doi:10.1158/1055-9965.Epi-03-0080 (2005).
- 873 58 Lee, J. E. *et al.* Statin use and colorectal cancer risk according to molecular
874 subtypes in two large prospective cohort studies. *Cancer Prev Res (Phila)* **4**,
875 1808-1815, doi:10.1158/1940-6207.CAPR-11-0113 (2011).
- 876 59 Kodach, L. L. *et al.* The effect of statins in colorectal cancer is mediated through
877 the bone morphogenetic protein pathway. *Gastroenterology* **133**, 1272-1281,
878 doi:10.1053/j.gastro.2007.08.021 (2007).
- 879 60 Andersen, C. L., Jensen, J. L. & Ørntoft, T. F. Normalization of real-time
880 quantitative reverse transcription-PCR data: a model-based variance
881 estimation approach to identify genes suited for normalization, applied to
882 bladder and colon cancer data sets. *Cancer research* **64**, 5245-5250,
883 doi:10.1158/0008-5472.Can-04-0496 (2004).
- 884 61 Bustin, S. A. *et al.* The MIQE guidelines: minimum information for publication
885 of quantitative real-time PCR experiments. *Clin Chem* **55**, 611-622,
886 doi:10.1373/clinchem.2008.112797 (2009).

- 887 62 Chen, S., Zhou, Y., Chen, Y. & Gu, J. fastp: an ultra-fast all-in-one FASTQ
888 preprocessor. *Bioinformatics* **34**, i884-i890, doi:10.1093/bioinformatics/bty560
889 (2018).
- 890 63 Dobin, A. *et al.* STAR: ultrafast universal RNA-seq aligner. *Bioinformatics* **29**,
891 15-21, doi:10.1093/bioinformatics/bts635 (2013).
- 892 64 Love, M. I., Huber, W. & Anders, S. Moderated estimation of fold change and
893 dispersion for RNA-seq data with DESeq2. *Genome Biology* **15**, 550,
894 doi:10.1186/s13059-014-0550-8 (2014).
- 895 65 Smedley, D. *et al.* BioMart – biological queries made easy. *BMC Genomics* **10**,
896 22, doi:10.1186/1471-2164-10-22 (2009).
- 897 66 Yu, G., Wang, L. G., Han, Y. & He, Q. Y. clusterProfiler: an R package for
898 comparing biological themes among gene clusters. *Omic* **16**, 284-287,
899 doi:10.1089/omi.2011.0118 (2012).
- 900 67 Liberzon, A. *et al.* The Molecular Signatures Database (MSigDB) hallmark gene
901 set collection. *Cell Syst* **1**, 417-425, doi:10.1016/j.cels.2015.12.004 (2015).
- 902 68 Gautier, L., Cope, L., Bolstad, B. M. & Irizarry, R. A. affy--analysis of Affymetrix
903 GeneChip data at the probe level. *Bioinformatics* **20**, 307-315,
904 doi:10.1093/bioinformatics/btg405 (2004).
- 905 69 Colaprico, A. *et al.* TCGAbiolinks: an R/Bioconductor package for integrative
906 analysis of TCGA data. *Nucleic Acids Res* **44**, e71, doi:10.1093/nar/gkv1507
907 (2016).
- 908 70 Subramanian, A. *et al.* Gene set enrichment analysis: a knowledge-based
909 approach for interpreting genome-wide expression profiles. *Proceedings of the*
910 *National Academy of Sciences of the United States of America* **102**, 15545-
911 15550, doi:10.1073/pnas.0506580102 (2005).
- 912 71 Wolf, F. A., Angerer, P. & Theis, F. J. SCANPY: large-scale single-cell gene
913 expression data analysis. *Genome Biol* **19**, 15, doi:10.1186/s13059-017-1382-
914 0 (2018).
- 915 72 Hao, Y. *et al.* Integrated analysis of multimodal single-cell data. *Cell* **184**, 3573-
916 3587.e3529, doi:<https://doi.org/10.1016/j.cell.2021.04.048> (2021).
- 917 73 Shannon, P. *et al.* Cytoscape: a software environment for integrated models of
918 biomolecular interaction networks. *Genome Res* **13**, 2498-2504,
919 doi:10.1101/gr.1239303 (2003).

920

921

922

923

924

925

926

927 **Conflict of interest.** The authors declare no conflict of interest.

928 **Acknowledgements.** This work was supported by the Cancer Prevention Research
929 Trust (CPRT), a CRUK programme grant (A13083) and a NIHR/CRUK-funded ECMC
930 grant [C325/A15575]. SW was funded by PhD fellowships from the CPRT (grant code
931 TM60003-CPRT and RM60G0499), I.G. was funded by a grant from the CPRT (grant
932 code RM60G0665-CPRT). P.R. was funded by a grant from the CPRT (grant code
933 RM60G0817). C.T. was supported by a Wellcome Trust Research Career Re-entry
934 Fellowship (210911/Z/18/Z, 'Exploiting transcription of repetitive DNA to study early
935 events in colorectal cancer'). R.P.G. was supported through a Development Grant to
936 A.R. and C.T. from the charity Hope Against Cancer
937 (<https://www.hopeagainstcancer.org.uk/>, grant code RM60G0751). We thank Dr Sara
938 Galavotti and Professor Andreas Gescher for critical reading of the manuscript. The
939 authors acknowledge the help from the staff of the Division of Biomedical Services,
940 Preclinical Research Facility, University of Leicester, for technical support and the care
941 of experimental animals. We thank the Advanced Imaging Facility
942 (RRID:SCR_020967) and the University of Leicester Core Biotechnology Services
943 Electron Microscopy Facility at the University of Leicester for support.

944 **Author contributions.**

945 A.R. and C.A.P designed the experiments. PR and RPG performed bioinformatics
946 analysis, S.W., P.F., H.C., I.G., S.U., L.S. G.C., E.P., H.J., F.H. and S.G. performed
947 the experiments. N.B.S. supported microarray and RNAseq experiments. N.S.A. and
948 A.S-I. performed electron microscopy. A.R, C.A.P, K.B., C.T. and R.F. analyzed the
949 data. AR and PR wrote the manuscript. All authors reviewed the manuscript.

950

951 **Figure legends**952 **Figure 1. Persistence of ISC and crypt hyperplasia in *Braf^{V600E}* intestinal tissue.**

953 **A)** Schematic of the experimental work: *VillinCre^{ER/0}/Braf^{V600E-LSL/+}* were culled 3 days
 954 and 6 months post induction of *Braf^{V600E}* for tissue histology and transcriptomic
 955 analysis. Mice were also culled at an intermediate time point 6 weeks post induction
 956 to corroborate changes in tissue histology. **B)** Violin plots showing the distribution of
 957 number of cells per crypt in control mice and mice induced with *Braf^{V600E}* for 3 days
 958 (BVE). Dotted and plain lines indicate median and quartiles respectively. Data were
 959 analyzed by Kolmogorov-Smirnov test. n=6 mice per group in 3 days, 4 WT and 3
 960 mutant mice in 6 weeks, n=4 mice per group in 6 months. 50 crypts were counted per
 961 each animal. ****P ≤ 0.0001. **C)** H&E representative images of hyperplastic crypts and
 962 quantification of proliferative cells (BrdU+) 3 days post tamoxifen injection. **D)** Violin
 963 plots showing the distribution of number of cells per crypt in mice induced for 6 weeks
 964 and 6 months plotted and analyzed as in A). ****P ≤ 0.0001. **E)** Histological images of
 965 small intestinal tissue stained with the stem cell marker Olfm4 from WT control mice
 966 and mice with the *Braf^{V600E}* mutation (BVE) at 3 days, 6 weeks and 6 months following
 967 tamoxifen induction. Bar size = 100 μm

968 **Figure 2. *Braf^{V600E}* expression in the intestinal epithelium alters intestinal**969 **homeostasis and affects absorptive and secretory cell lines. A)** GSEA showing

970 changes in differentiation gene signatures 3 days and 6 months following tamoxifen

971 induction. NES = normalized enrichment score. **B)** GSEA showing changes in an

972 enterocyte gene signatures 6 months following tamoxifen induction. NES = normalized

973 enrichment score. **C)** Histological images of small intestinal tissue from WT control

974 mice and mice with the *Braf^{V600E}* mutation (BVE) 6 months following tamoxifen

975 induction stained with alkaline phosphate (Alpl) to assess enterocyte cells. **D)** TEM

976 images of WT and *Braf* mutant intestinal tissues showing altered microvilli in mutant
 977 mice. scale bar = 1 μ m. **E)** Quantification of Goblet and ChgA+ enteroendocrine cells
 978 from the indicated mice. Each dot represents a single mouse and lines represent mean
 979 \pm SEM. Data were analyzed by unpaired two-tailed t-test (n=3 per group). *P \leq 0.05,
 980 **P \leq 0.001. **F)** rt-qPCR analysis of the expression of the intestinal biomarkers
 981 Chromogranin A, (*ChgA*, EECs) 6 months after induction of *Braf*^{V600E}. Data are plotted
 982 as mean \pm SD and were analyzed by unpaired two-tailed t-test (n=4 per group). *P \leq
 983 0.05.

984 **Figure 3. Expression of *Braf*^{V600E} in the intestinal epithelium induces persistent**
 985 **gene signatures related to CRC. A)** GSEA showing changes in signatures
 986 associated with *BRAF*^{V600E}-driven CRC (WT vs *Braf*^{V600E}) 3 days and 6 months
 987 following tamoxifen induction. NES = normalized enrichment score. **B)** GSEA showing
 988 changes in the Wnt signatures 3 days and 6 months following tamoxifen induction.
 989 NES = normalized enrichment score. **C)** GSEA showing enrichment in a poor-
 990 prognosis gene signature for *BRAF*^{V600E}-drive CRC 6 months following tamoxifen
 991 induction. NES = normalized enrichment score. **D)** GSEA showing dependence on
 992 MAPK pathway for the establishment of key gene signatures. Mice expressing
 993 *Braf*^{V600E} for 3 days were treated with vehicle control or the MEK inhibitor PD184352
 994 (MEKi). NES = normalized enrichment score.

995 **Figure 4. *Braf*^{V600E} in the intestinal epithelium shows enriched expression of a**
 996 **gene signature related to cholesterol metabolism. A)** GSEA showing changes in
 997 gene expression of the cholesterol biosynthesis signature 3 days and 6 months
 998 following tamoxifen induction. NES = normalized enrichment score. **B)** Treatment of
 999 mice with the MEK inhibitor PD184352 reverts the enrichment of the cholesterol
 1000 biosynthesis gene signature in intestinal tissue. NES = normalized enrichment score.

1001 **C)** rt-qPCR analysis of cholesterol metabolism genes in intestinal tissue collected 6
 1002 months after tamoxifen injection. Data are reported as fold over WT control mice. Bars
 1003 represent mean \pm SEM. Data were analyzed by unpaired two-tailed t-test (n=4 per
 1004 group). **P \leq 0.01; ***P \leq 0.001. **D)** GSEA showing increased transcriptional
 1005 expression of cholesterol biosynthesis gene signature in the intestinal tissue of two
 1006 independent *Braf*^{V600E} mouse datasets. NES = normalized enrichment score. **E)** Violin
 1007 plot showing the distribution of number of cells per crypt in *Braf* mutant mice induced
 1008 for 3 days and treated with vehicle control or atorvastatin 10 mg/mL. Dotted and plain
 1009 lines indicate median and quartiles respectively. Data were analyzed by Kolmogorov-
 1010 Smirnov test. n=6 mice in the vehicle group and 3 mice in the atorvastatin-treated
 1011 group. 50 crypts were counted per each animal **P \leq 0.01. **F)** and **G)** Cell proliferation
 1012 and apoptosis were evaluated in *Braf* mutant intestinal crypts of mice treated with
 1013 vehicle control or atorvastatin using IHC for BrdU and cleaved-PARP1, respectively.
 1014 Examples of cleaved-PARP positive crypt cells are provided. Data are plotted as box
 1015 and whiskers plots. Whiskers represent min and max value. Data were analyzed using
 1016 unpaired, two-tailed t-test (n=6 vehicle and 3 atorvastatin treated animals). Ns = no
 1017 significant ****P \leq 0.0001.

1018 **Figure 5. Gene signatures of cholesterol biosynthesis are enriched in**
 1019 **transcriptomic datasets of human colorectal neoplasia. A) and B)** GSEA showing
 1020 increased expression of the cholesterol gene signature in human SSLs from 3
 1021 independent datasets comparing SSLs to normal matched control (A) or to
 1022 adenomatous lesions (B). **C)** UMAP visualization of cells from SSL and NL dataset
 1023 colored by annotated cell type. ABS, absorptive cells; CT, crypt top colonocytes; EE,
 1024 enteroendocrine cells; GOB, goblet cells; SSC, serrated specific cells; STM, stem
 1025 cells; TAC, transient amplifying cells; TUF, tuft cells **D)** UCell score distribution for the

1026 cholesterol gene signature shown in UMAP space. **E)** Violin plot showing a
 1027 comparison of UCell score distribution of a cholesterol gene signature in different cell
 1028 populations. Distribution of UCell score in SSC population was compared with
 1029 remaining cell lineages using Wilcoxon statistical test. **** $P \leq 0.0001$.

1030 **Figure 6. A)** Regulon activity projected in UMAP space for the regulons associated
 1031 with transcription factors (FOSL1, SP6, KLF16, NR2F1, CEBPB, CREB3) involved in
 1032 the establishment of the cholesterol gene signature in the SSCs. **B)** A network diagram
 1033 generated with iRegulon in Cytoscape using the differentially expressed gene of the
 1034 cholesterol biosynthesis signature in SSC identified by Seurat as an input. Circles
 1035 indicate 21 significant genes, colored by avg_Log2FC. Octagons symbolizes selected
 1036 TFs (cut off > 5 target genes) involved in the regulation of DEGs in the cholesterol
 1037 biosynthesis signature. The edges represent connections between each of six TFs
 1038 and their target genes, and are colored based on the source of integration.

1039 **Supplemental Figure legends**

1040 **Supplemental Figure 1. Expression of *Braf^{V600E}* in the intestinal epithelium**
 1041 **reduces animal lifespan and generates limited tumorigenesis. A)** Kaplan-Meyer
 1042 survival analysis showing reduced survival of *Braf^{V600E}* mice (median survival 622 days
 1043 and 414 days, $P < 0.0001$ Mantel-Cox Log-rank test). **B)** Graph showing the number of
 1044 tumors in mice culled at the indicated time post-tamoxifen injection. **C)** H&E
 1045 representative images of intestinal tissue hyperplasia (HP) and intestinal lesions.
 1046 LGD=low grade dysplasia, HGD=high grade dysplasia, Ca=cancer.

1047 **Supplemental Figure 2. Transcriptomic analysis of mice after short term (3 days)**
 1048 **and long-term (6 months) induction of the *Braf^{V600E}* oncogene. A)** Principal
 1049 component analysis (PCA) of *Braf^{V600E}* mice and WT controls showing clustering by

1050 genotype. n=6 animals per genotype. **B)** Volcano plot of differentially expressed genes
1051 in *Braf^{V600E}* versus WT control mice. Log2 for fold change in expression on the X-axis
1052 and Log10 for adjust P value on Y-axis. Results are color coded: adjusted p value less
1053 than 0.05 (grey), log2 fold change greater than 0.5 (green), adjusted p value less than
1054 0.05 (blue), and both adjusted p value less than 0.05 and log2 fold change greater
1055 than 0.5 (red). **C)** Heat map with the most top significantly up and down regulated
1056 genes in *Braf^{V600E}* intestine.

1057 **Supplemental Figure 3.** GSEA showing persistent enrichment of a MAPK signature
1058 in the intestinal tissue of *Braf^{V600E}* mice. NES = normalized enrichment score.

1059 **Supplemental Figure 4. Persistence of ISCs following expression of *Braf^{V600E}* in**
1060 **intestinal tissue. A)** rt-qPCR analysis of intestinal stem cells biomarkers *Lgr5* and
1061 *Olfm4* 6 months after tamoxifen injection. Each dot represent a single mouse and lines
1062 represent mean \pm SEM. Data were analyzed by unpaired two-tailed t-test (n=4 per
1063 group). ns = not significant. **B)** GSEA 3 days and 6 months after induction of mutant
1064 *Braf* showing changes in the expression of an intestinal stem cells signature. NES =
1065 normalized enrichment score.

1066 **Supplemental Figure 5. Expression of *Braf^{V600E}* in the intestinal epithelium alters**
1067 **homeostasis of Paneth cells. A)** Representative histological images of small
1068 intestinal tissue stained with the lysozyme marker from WT mice and *Braf^{V600E}* mice
1069 (BVE) at 3 days, 6 weeks and 6 months following tamoxifen induction. Bar size = 100
1070 μ m. **B)** Details of delocalized Paneth cells in 6-month induced mutant mice. Bar size
1071 = 100 μ m (20 μ m inset). **C)** rt-qPCR analysis of the expression of the Paneth cell
1072 marker Lysozyme 6 months after induction of *Braf^{V600E}*. Data are plotted as mean \pm
1073 SD and were analyzed by unpaired two-tailed t-test (n=4 per group). *P \leq 0.05.

1074 **Supplemental Figure 6. Expression of *Braf*^{V600E} in the intestinal epithelium alters**
1075 **intestinal tissue homeostasis. A)** Representative histological images of small
1076 intestinal tissue from WT mice and *Braf*^{V600E} mice (BVE) at 3 days, 6 weeks and 6
1077 months following tamoxifen induction. Bar size = 100 μ m. **B)** Bar graph showing
1078 quantification of villi length in mice 3 days, 6 weeks and 6 months following tamoxifen
1079 induction. Data are plotted as mean \pm SEM. Data were analyzed by unpaired two-
1080 tailed t-test (n=3 per group). ***P \leq 0.001, ****P \leq 0.0001.

1081 **Supplemental Figure 7. Expression of *Braf*^{V600E} in the intestinal epithelium alters**
1082 **homeostasis of EE cells.** Representative histological images of small intestinal tissue
1083 stained with Alcian Blue (Goblet cells) and the EEC marker ChgA in the intestinal
1084 tissue of mice with the indicated genotypes. Independent WT mice were used for each
1085 different time point, but, for ease of reference, representative examples from 6 months
1086 mice are shown. Bar size = 100 μ m.

1087 **Supplemental Figure 8. GSEA of mouse transcriptomic data. A)** and **B)** most
1088 significant up and down regulated signatures from the MSigDB in *Braf*^{V600E} mice at 3
1089 days (A) and 6 months (B) following induction of mutant *Braf*.

1090 **Supplemental Figure 9. Analysis of the TCGA transcriptomic dataset.** GSEA
1091 analysis shows significant enrichment of the Myc targets, E2F targets and G2M
1092 checkpoint signatures. NES = normalized enrichment score.

1093 **Supplemental Figure 10. Inhibition of MAPK pathway with the MEK inhibitor**
1094 **PD1843352. A)** Schematic of the experimental design for *in vivo* inhibition of the
1095 MAPK pathway using the pharmacological inhibitor PD184352. **B)** Western blot
1096 analysis of phosphorylated Erk protein in intestinal tissue showing efficient inhibition
1097 of the MAPK pathway in mice treated with the MEK inhibitor PD184352 (MEKi). **C)**

1098 Principal component analysis (PCA) of *Braf*^{V600E} mice treated with MEKi or vehicle.
1099 n=6 animals per genotype. **D)** Volcano plot of differentially expressed genes in
1100 *Braf*^{V600E} treated with MEKi versus vehicle control mice. Log2 for fold change in
1101 expression on the X-axis and Log10 for adjust P value on Y-axis. Results are color
1102 coded: adjusted p value less than 0.05 (grey), log2 fold change greater than 0.5
1103 (green), adjusted p value less than 0.05 (blue), and both adjusted p value less than
1104 0.05 and log2 fold change greater than 0.5 (red). **E)** Heat map with the most top
1105 significantly up and down regulated genes in *Braf*^{V600E} mice treated with MEKi. **F)**
1106 GSEA showing downregulation of MAPK pathway signature in mice expressing
1107 *Braf*^{V600E} for 3 days and treated with the MEK MEKi. NES = normalized enrichment
1108 score.

1109 **Supplemental Figure 11. Expression of *Braf*^{V600E} in the mouse intestinal**
1110 **epithelium leads to enrichment of a fetal-like gene signature. A)** GSEA of the fetal
1111 and metaplasia gene signatures in two independent human dataset comparing SSLs
1112 to tubular adenomas or matched normal tissue. **B)** GSEA of the fetal signature the
1113 intestinal tissue of *Braf*^{V600E} mice 3 days and 6 months following induction of mutant
1114 *Braf*. Dependence on MAPK is also shown. NES = normalized enrichment score.

1115 **Supplemental Figure 12. Expression of metaplastic genes *Aqp5* and *Anxa10* in**
1116 **intestinal tissue of mice with the *Braf*^{V600E} mutation.** Normalized expression levels
1117 of the *Aqp5* and *Anxa10* genes in the intestinal tissue at the indicated time points.
1118 Dependence on MEKi is also shown. P value was determined using Wald test. Data
1119 are plotted as box and whiskers plots. The bar within the box represent the median
1120 value, whiskers represent min and max value.

1121 **Supplemental Figure 13. Analysis of human transcriptomic datasets. A)** GSEA
1122 shows lack of transcriptional enrichment of the cholesterol gene signature in
1123 adenomas lesions compared to match normal tissue.

1124 **Supplemental Figure 14. Single cells analysis of cholesterol biosynthesis in**
1125 **SSLs. A)** UMAP representation of epithelial scRNA-seq data, color-coded by cell type
1126 and comparing cell population in, normal tissue (NL), SSL, sessile serrated lesions.
1127 ABS, absorptive cells; CT, crypt top colonocytes; EE, enteroendocrine cells; GOB,
1128 goblet cells; SSC, serrated specific cells; STM, stem cells; TAC, transient amplifying
1129 cells; TUF, tuft cells. **B)** Dot plot of genes within the cholesterol signature showing
1130 significant upregulation in gene expression between SSC and non-tumor cells. Dot
1131 color indicates average gene expression levels, dot size indicates the percentage of
1132 cells within a population that express the indicated gene.

1133 **Supplemental Figure 15. Analysis of regulons in SSLs.** Plot of the top 30 specific
1134 regulons (highlighted in red) in the indicated cell lines from analysis of single cell
1135 data of SSL and NL dataset. The regulon specificity score (RSS) is shown on y axis.
1136 ABS, absorptive cells; CT, crypt top colonocytes; EE, enteroendocrine cells; GOB,
1137 goblet cells; SSC, serrated specific cells; STM, stem cells; TAC, transient amplifying
1138 cells; TUF, tuft cells.

1139 **Supplemental Figure 16. The effects of cholesterol biosynthesis inhibition on**
1140 **cell viability in *BRAF*^{V600E} colorectal cancer cells.** The effect of different
1141 concentrations (0, 5 and 10 μ M) of atorvastatin and periods of treatment (24, 48 and
1142 72 hrs) on RKO (A) and HT-29 (B) cell lines. Values were normalized against the
1143 control mean by dividing the measured optical density by the mean control optical
1144 density and multiplying by 100 to give cell viability as a percentage of the control.

1145 The error bars represent standard error of the mean (SEM). Results were obtained
1146 from two independent experiments. Significance levels were measured against the
1147 controls for each treatment period and between treatment concentrations for each
1148 treatment period using a two-way ANOVA and Tuckey post hoc analysis * $p < 0.05$,
1149 ** $p < 0.01$, *** $p < 0.005$, **** $p < 0.001$.

1150

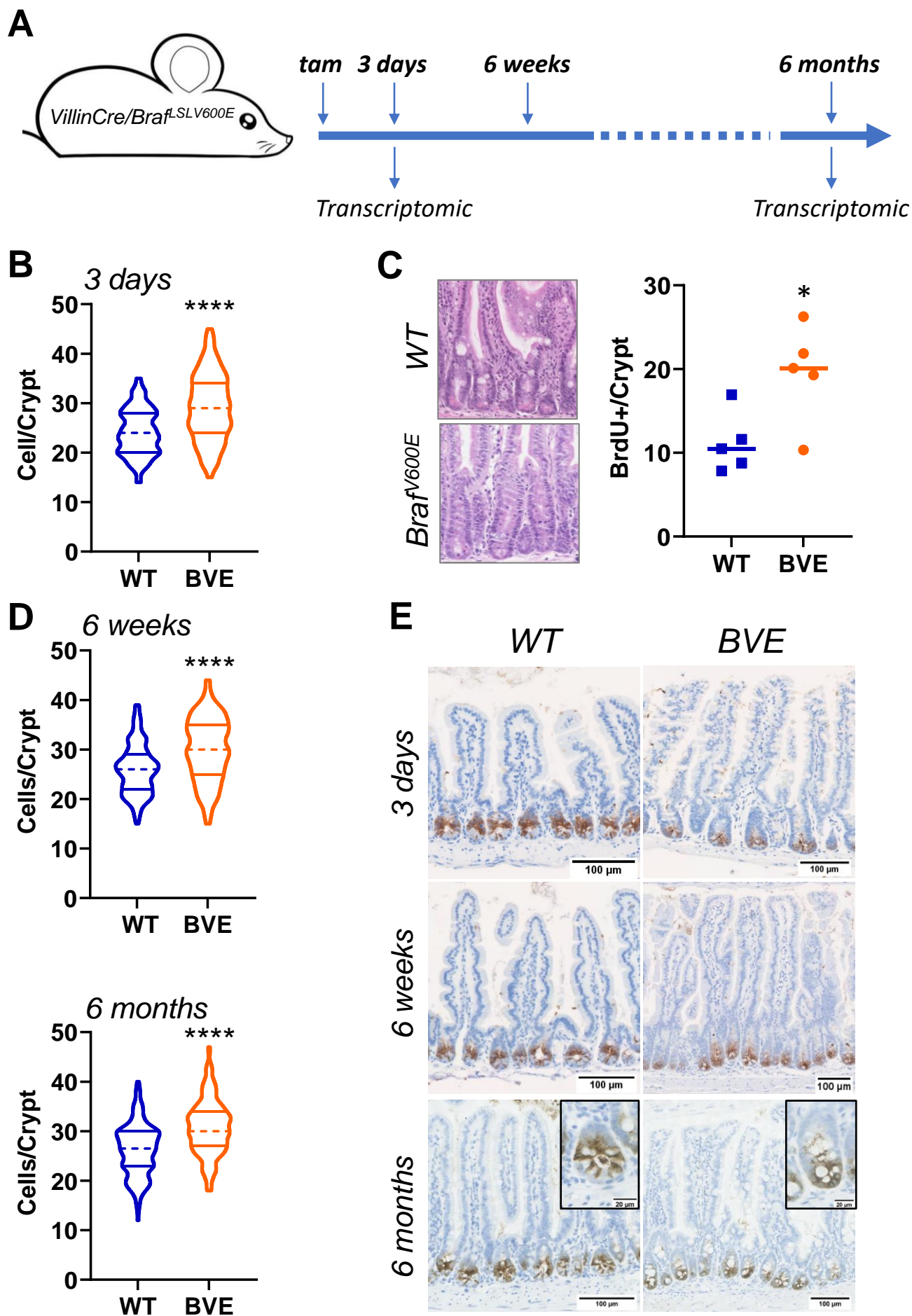
Figure 1

Figure 2

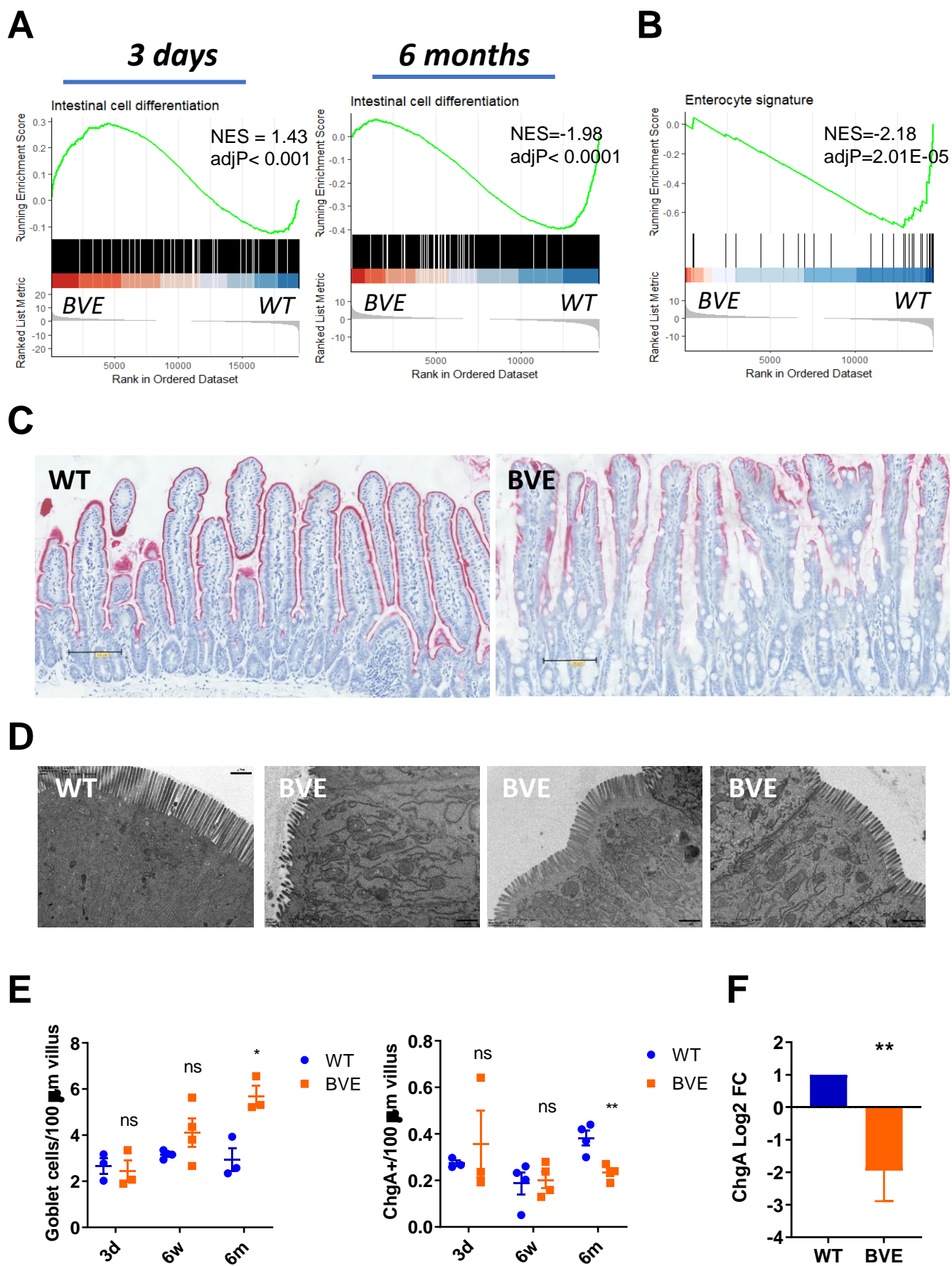


Figure 3

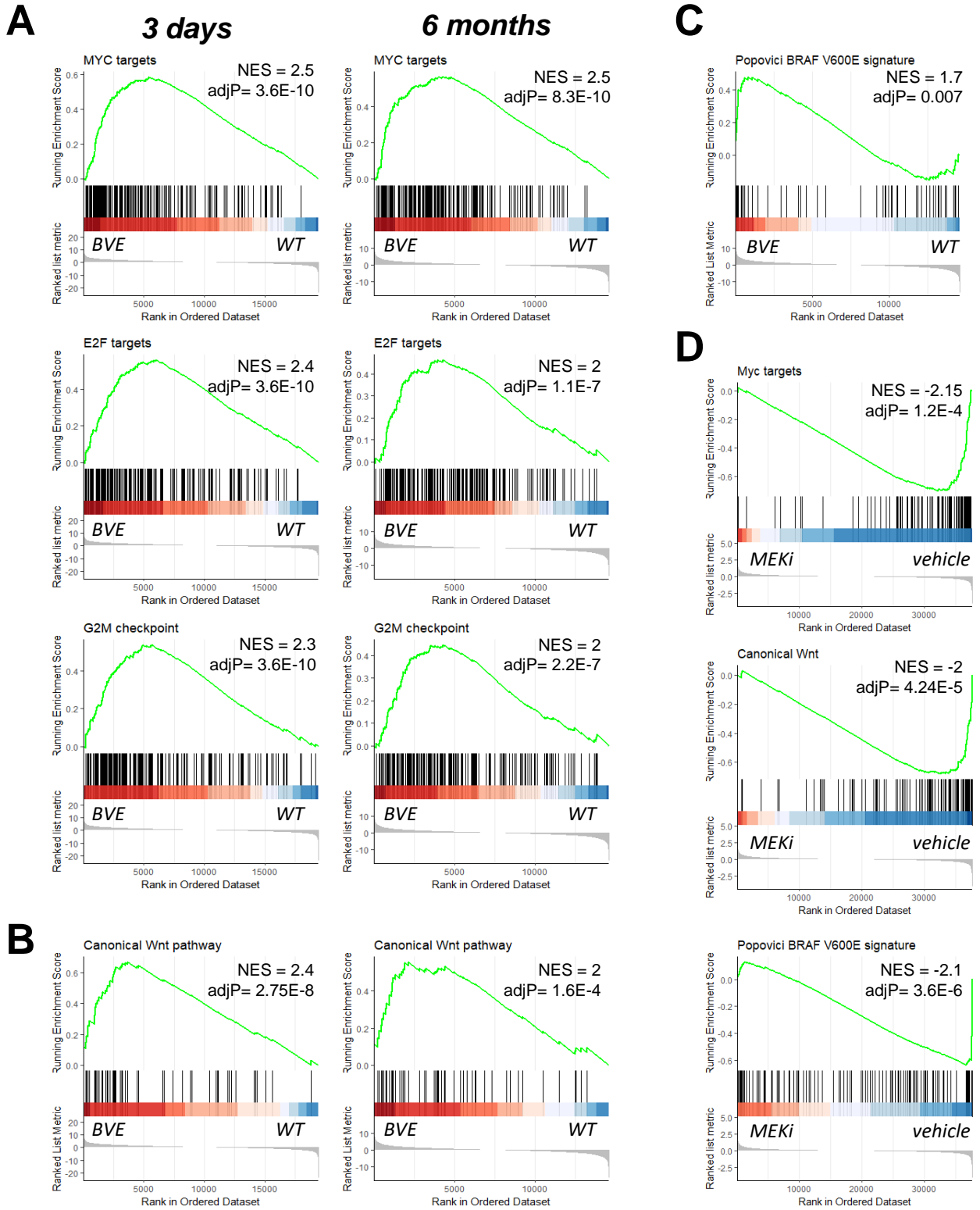
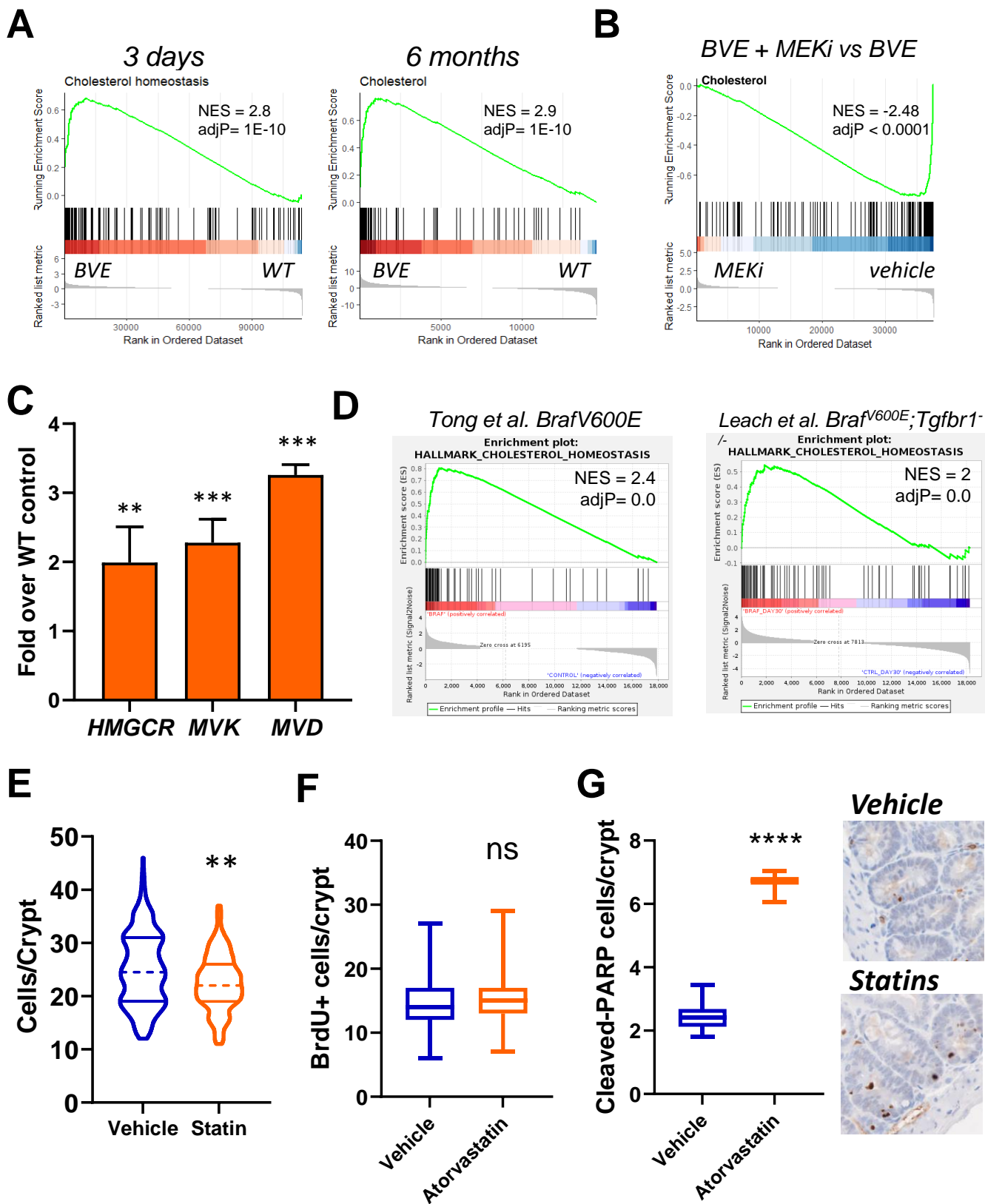
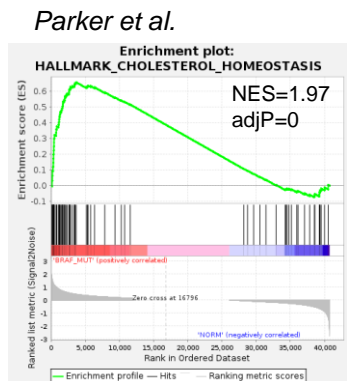


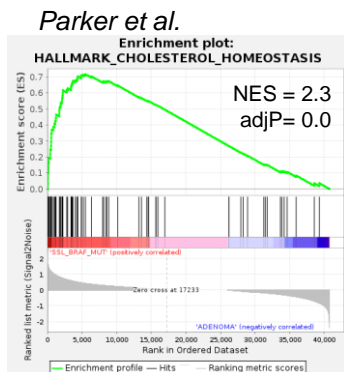
Figure 4



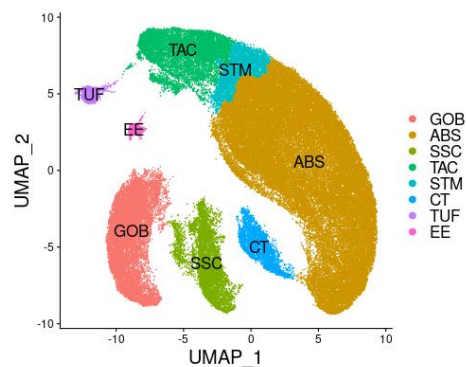
A SSL vs normal colon



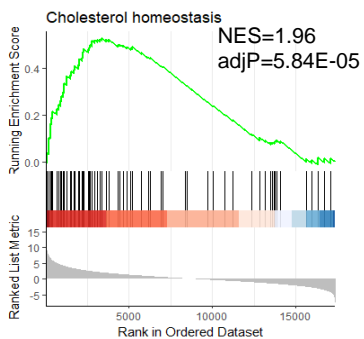
B SSL vs ADs



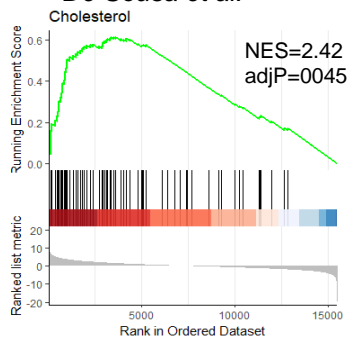
C



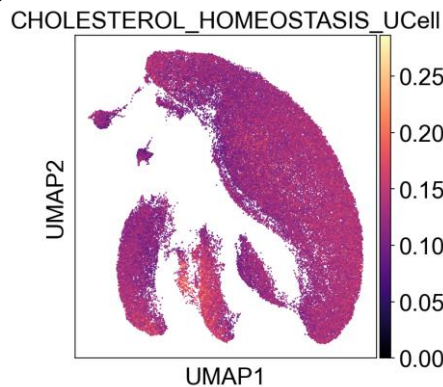
Delker et al.



De Sousa et al.



D



E

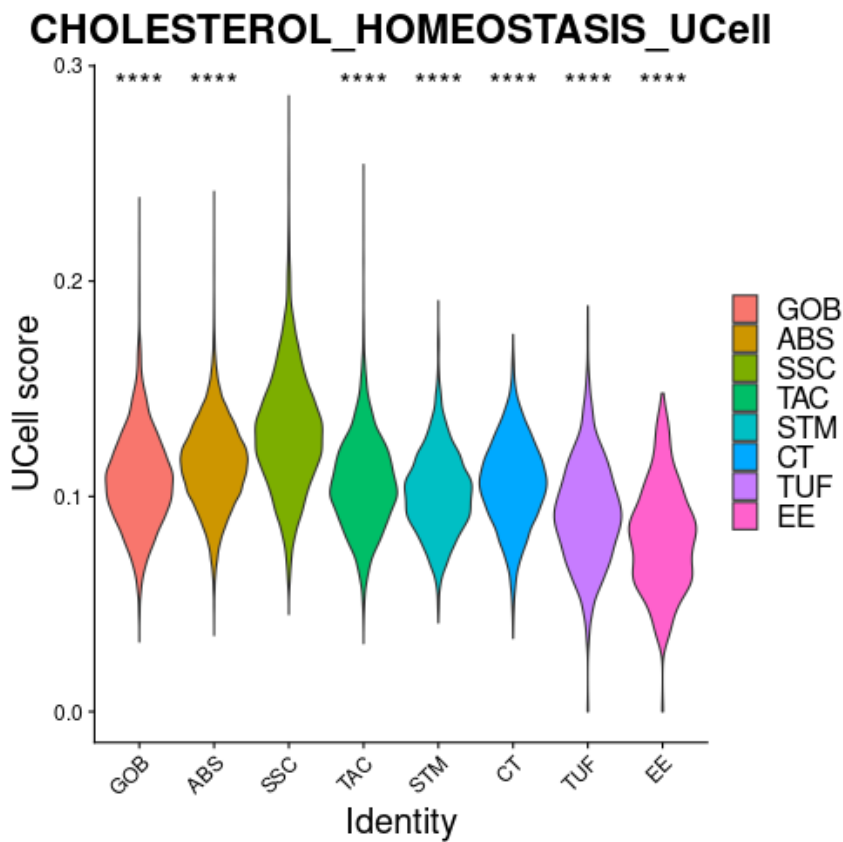
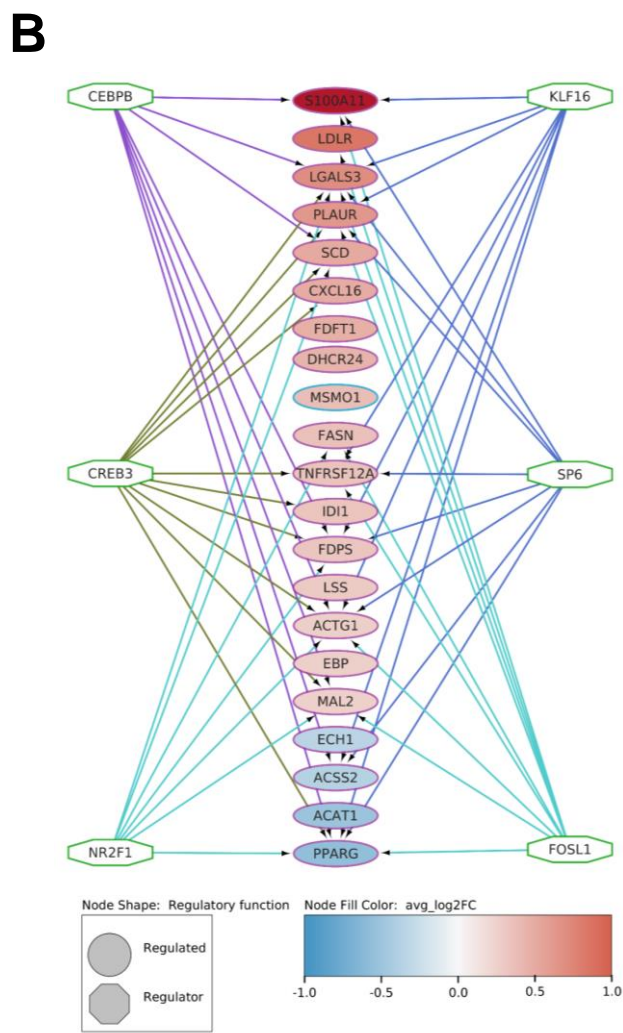
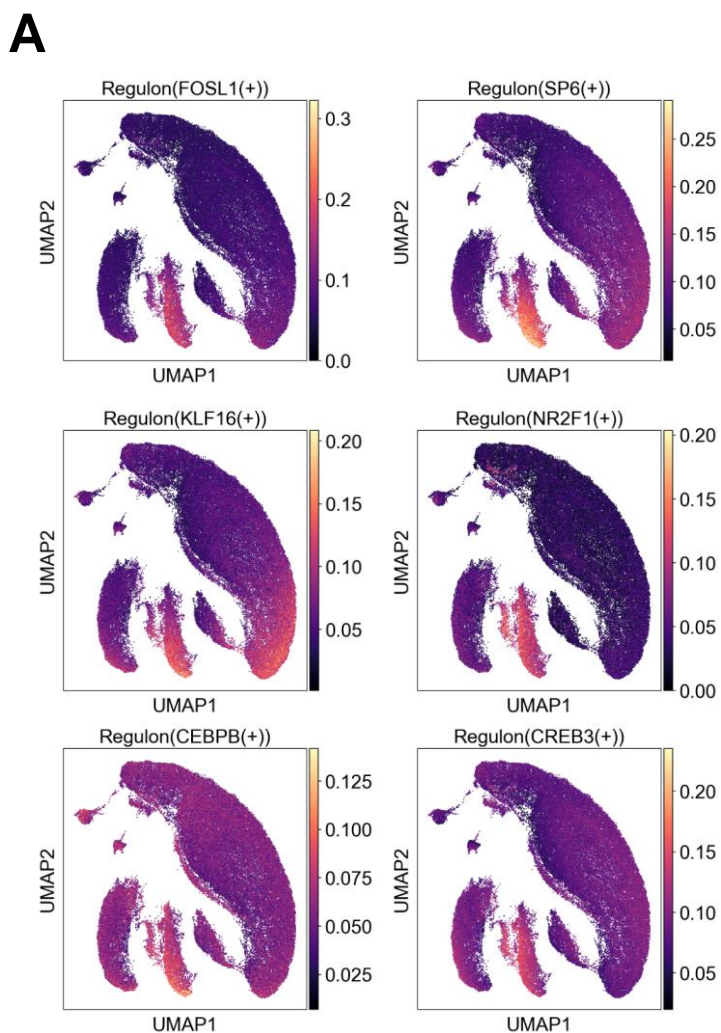
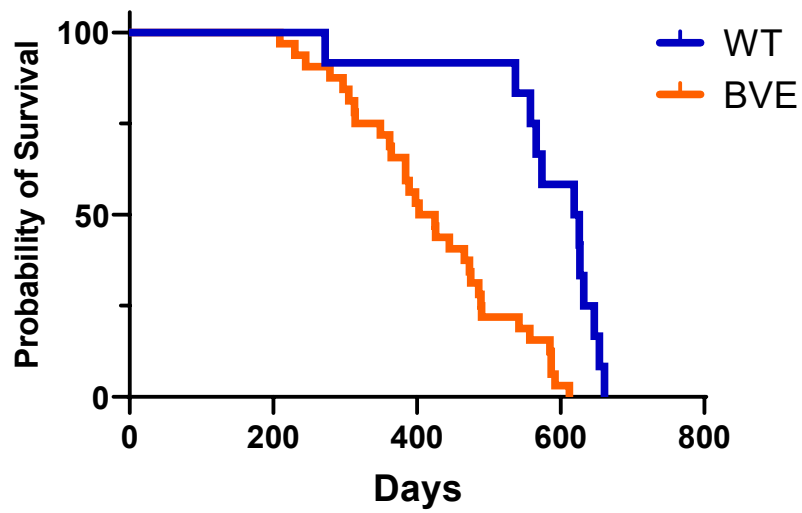


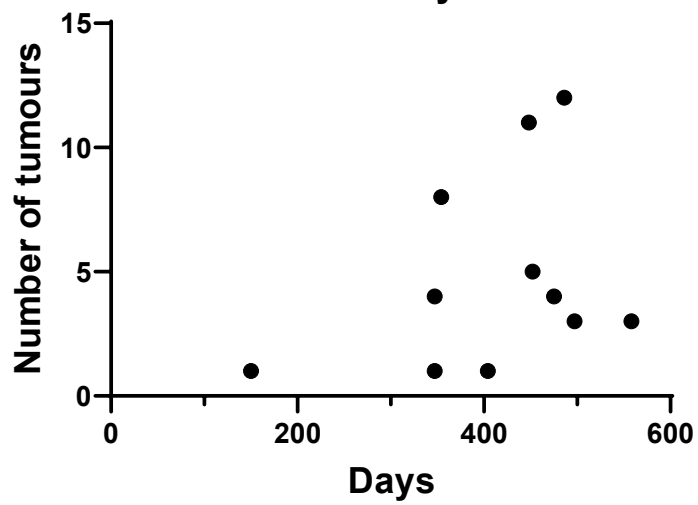
Figure 6



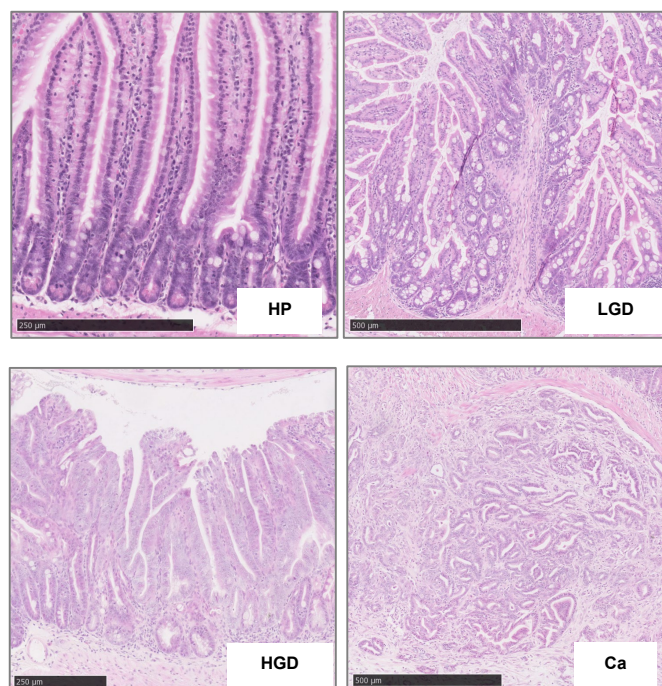
A



B

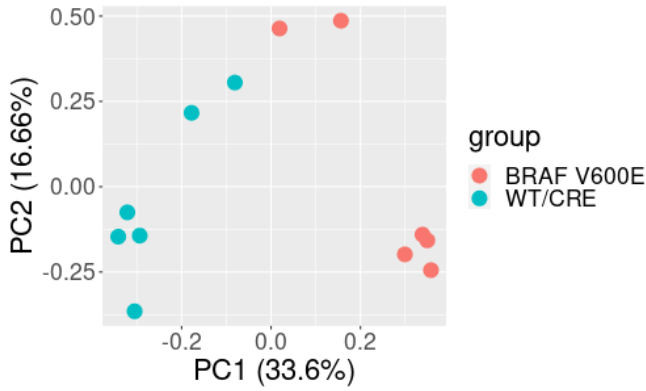


C

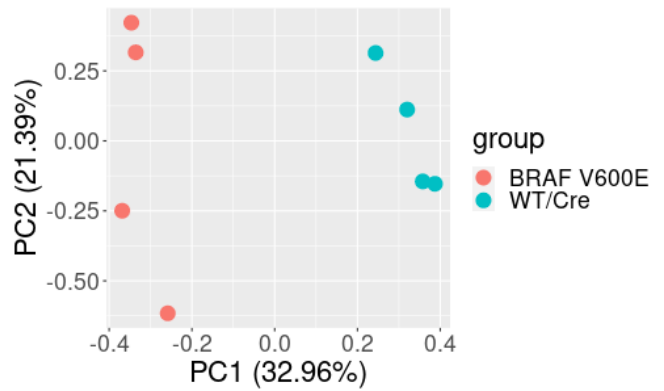


A

3 days mice



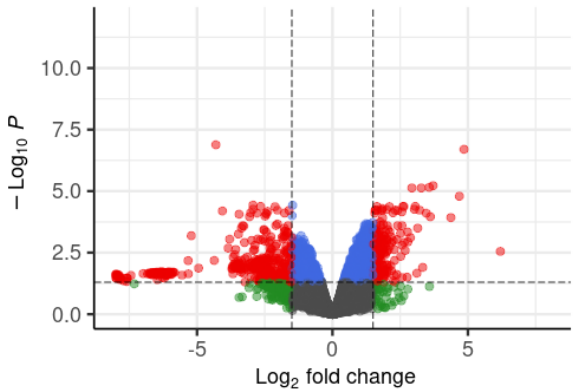
6 months mice



B

3d

Differential expression

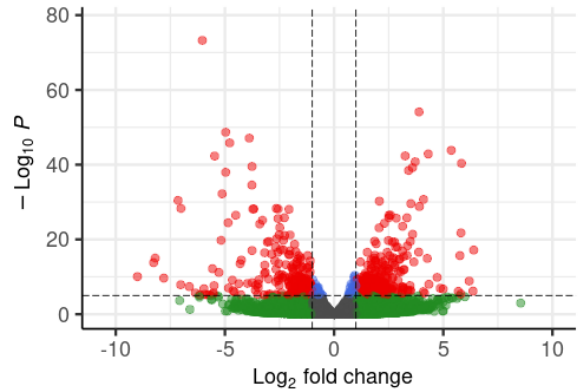


● NS ● Log₂ FC ● p-value ● p-value and log₂ FC

total = 62976 variables

6m

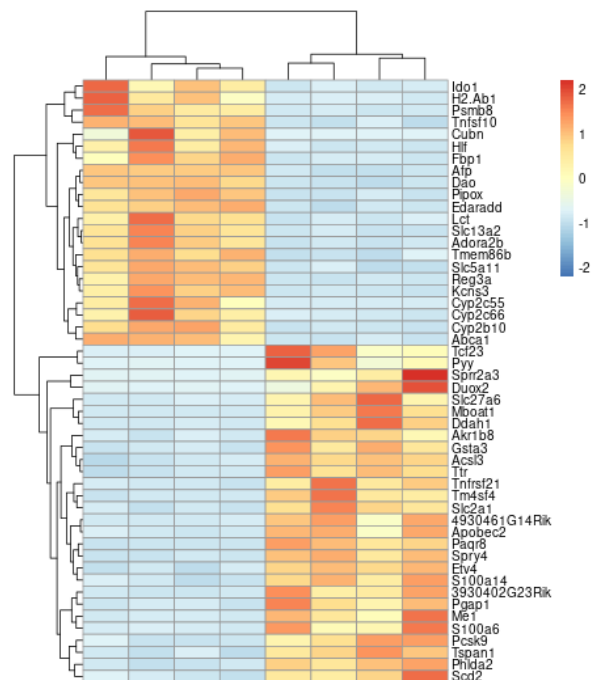
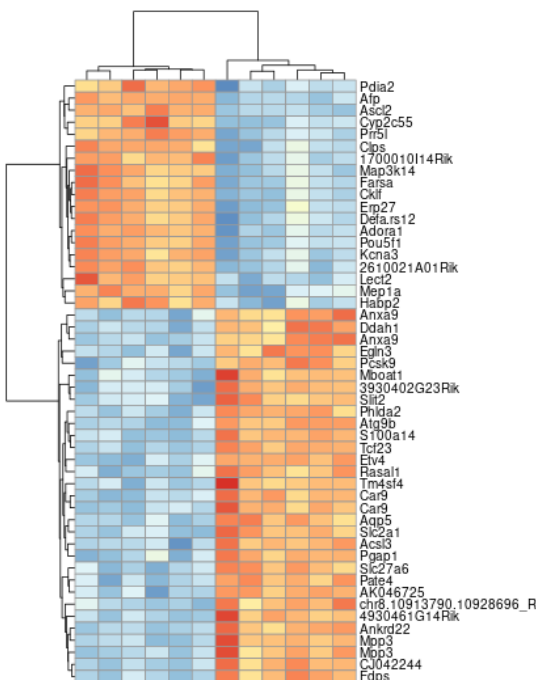
Differential expression



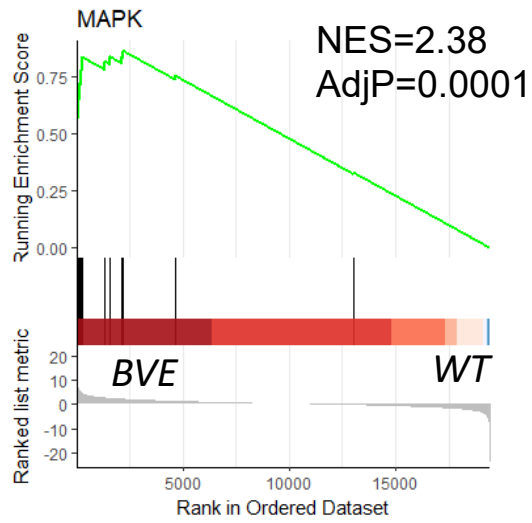
● NS ● Log₂ FC ● p-value ● p-value and log₂ FC

total = 55414 variables

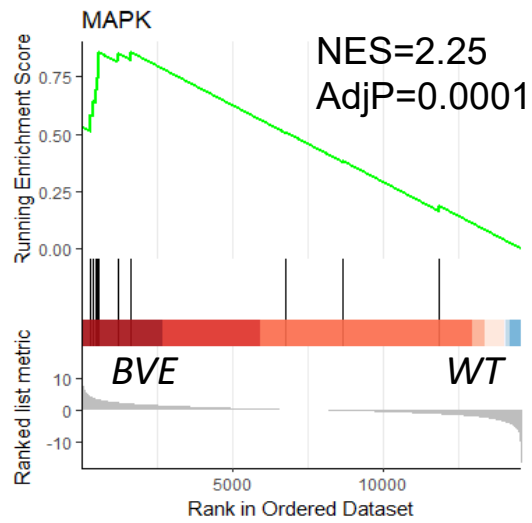
C



3 days

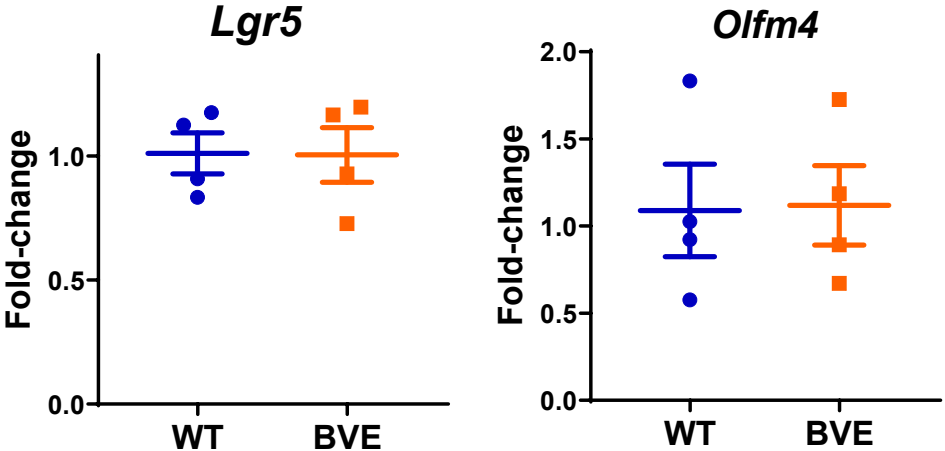


6 months

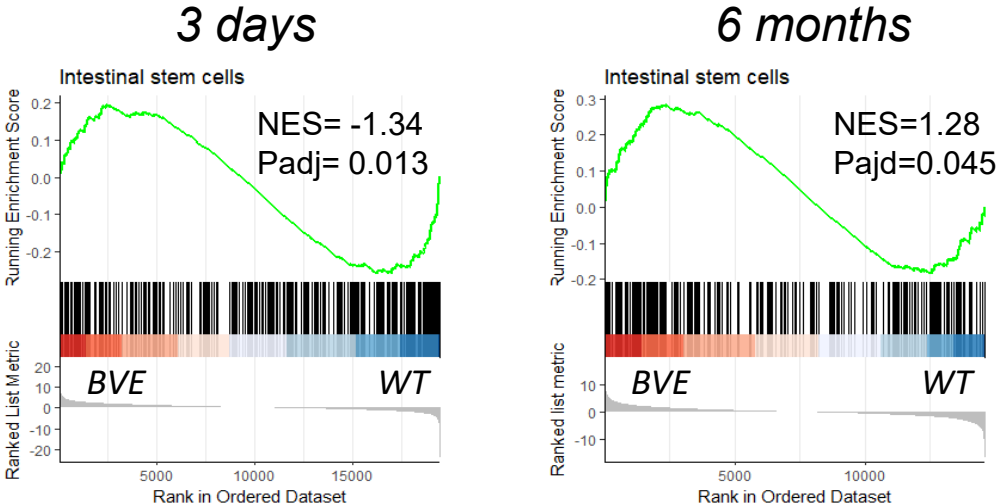


Supplemental Figure 4

A

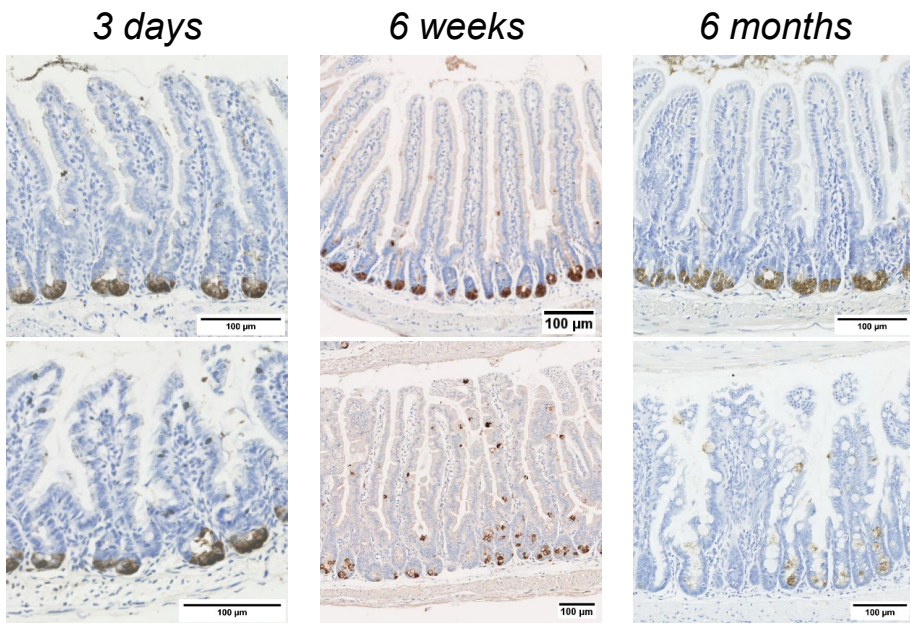


B

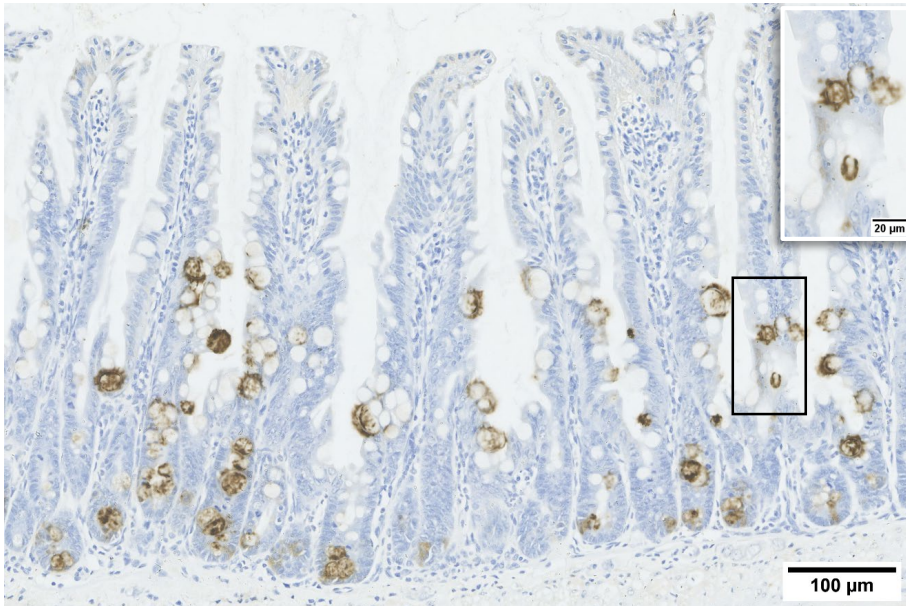


Supplemental Figure 5

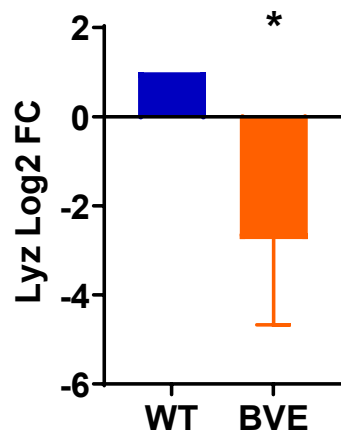
A



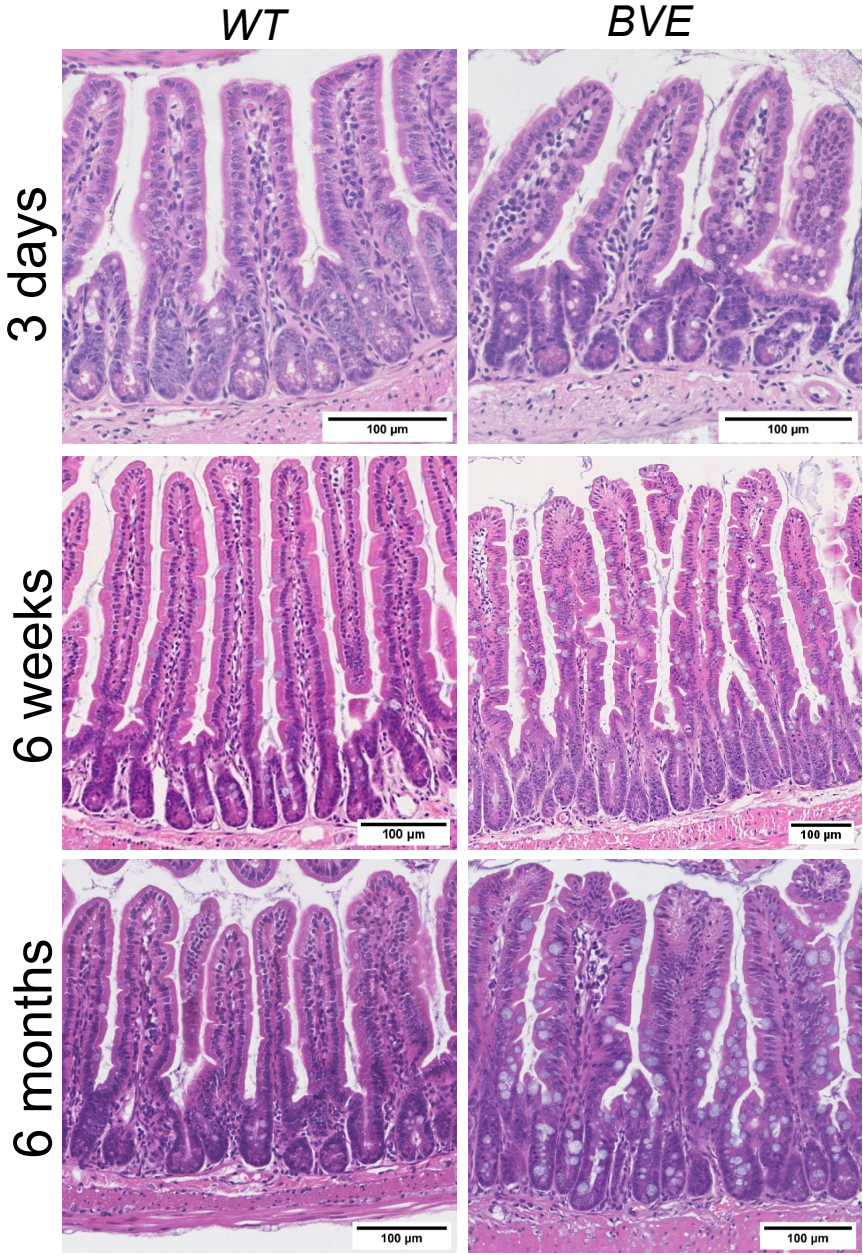
B



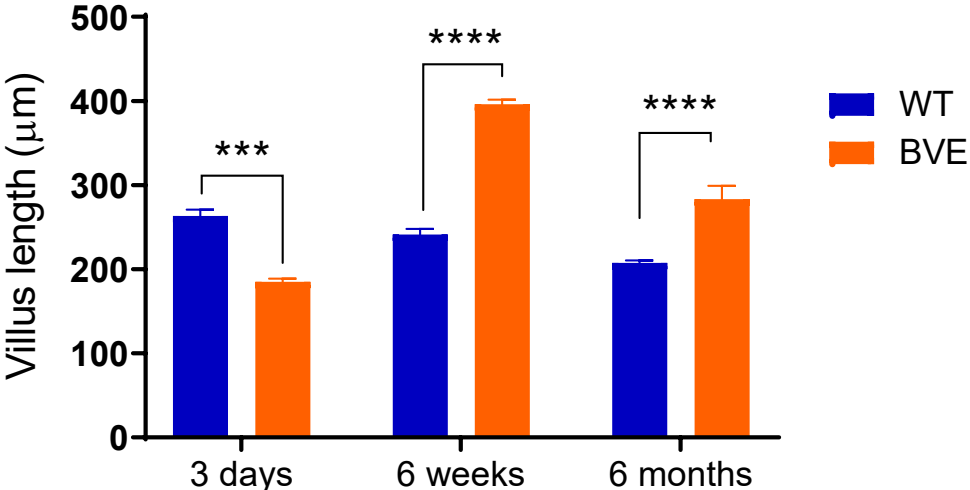
C



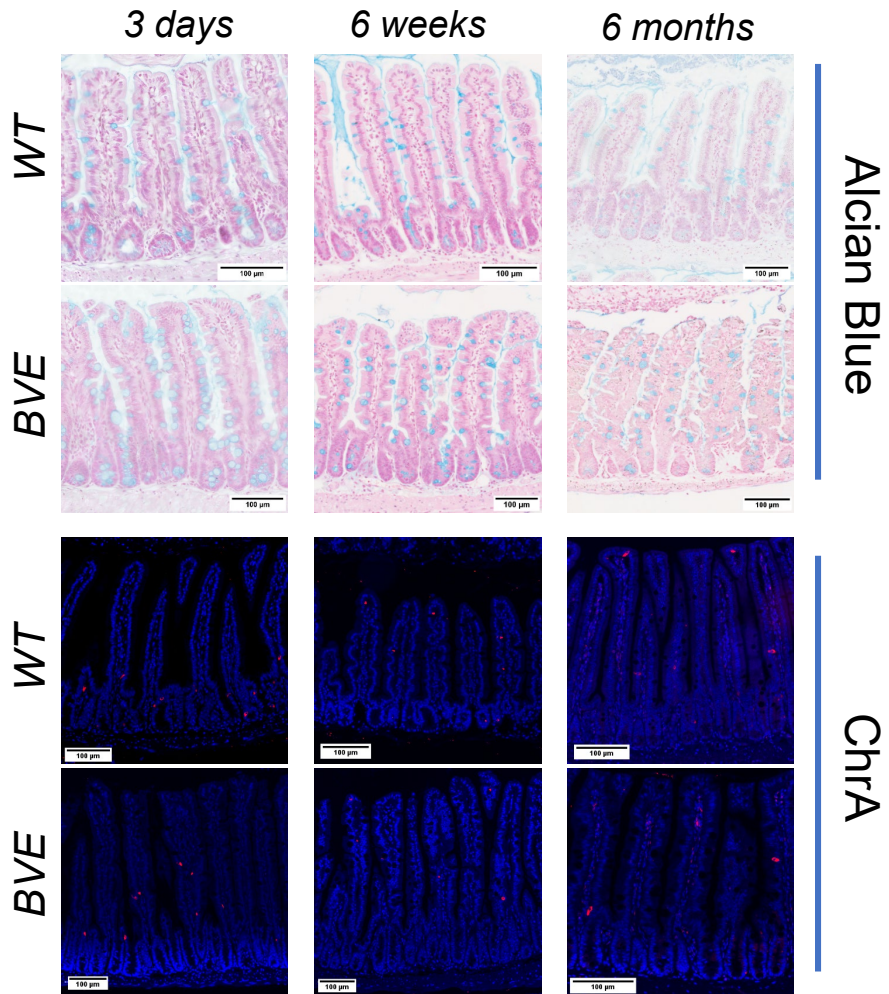
A



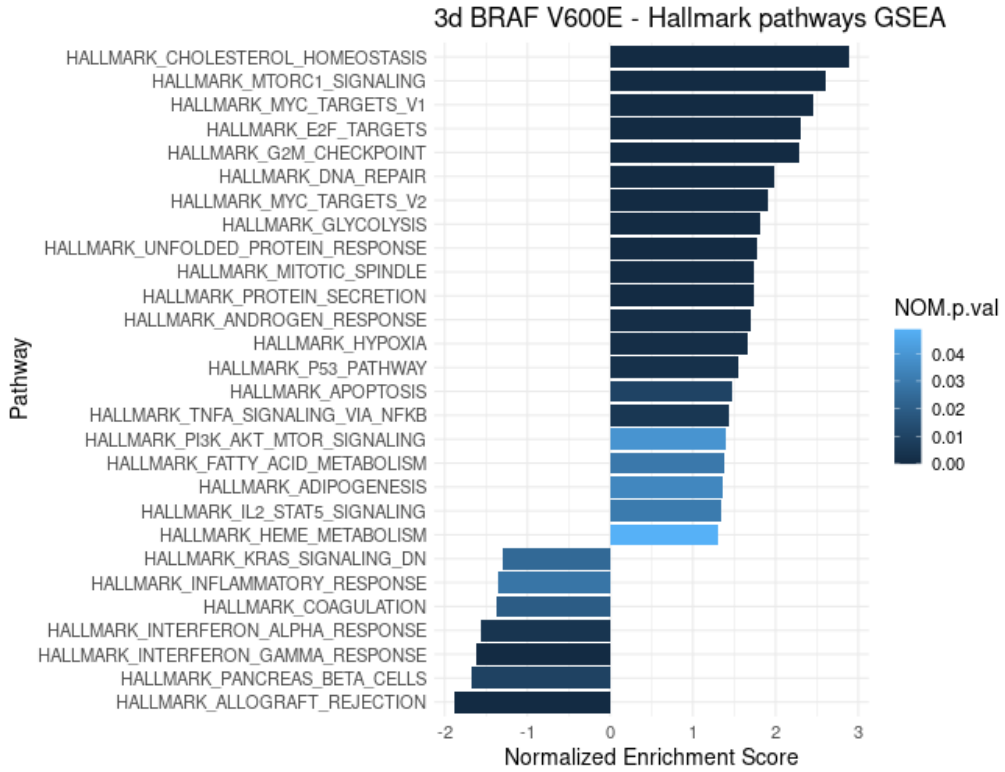
B



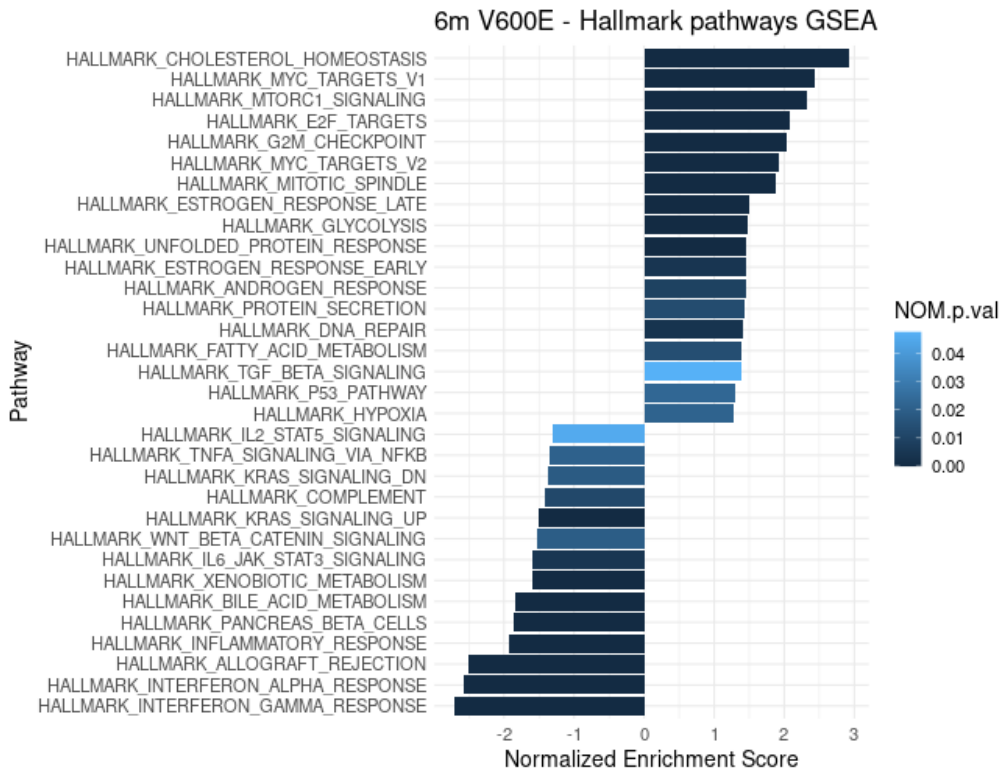
Supplemental Figure 7



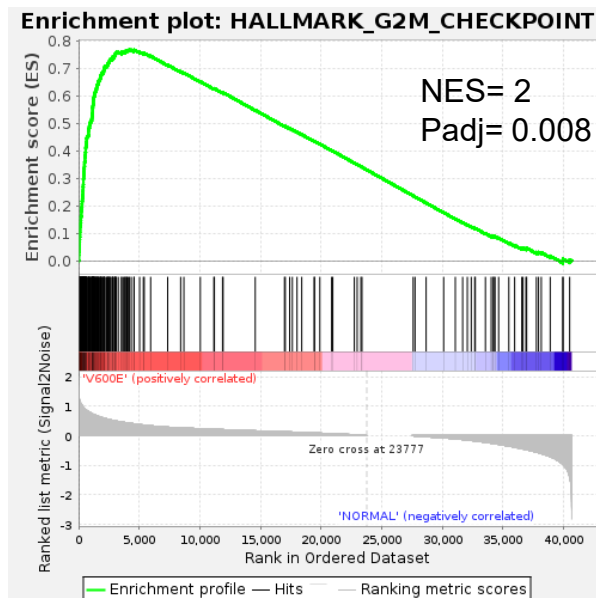
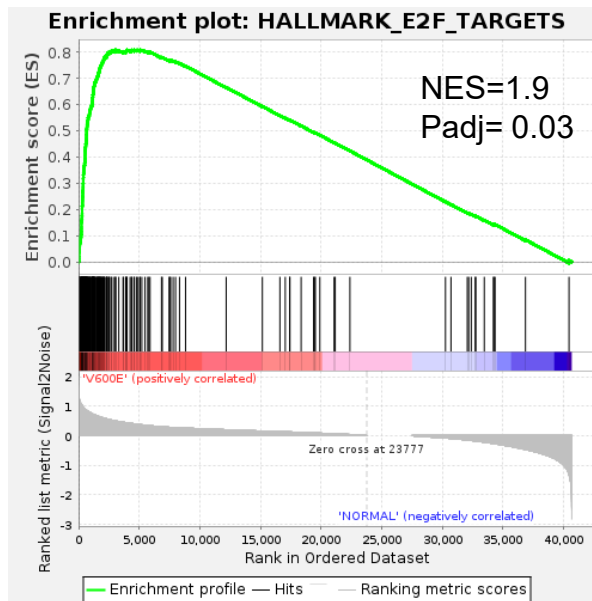
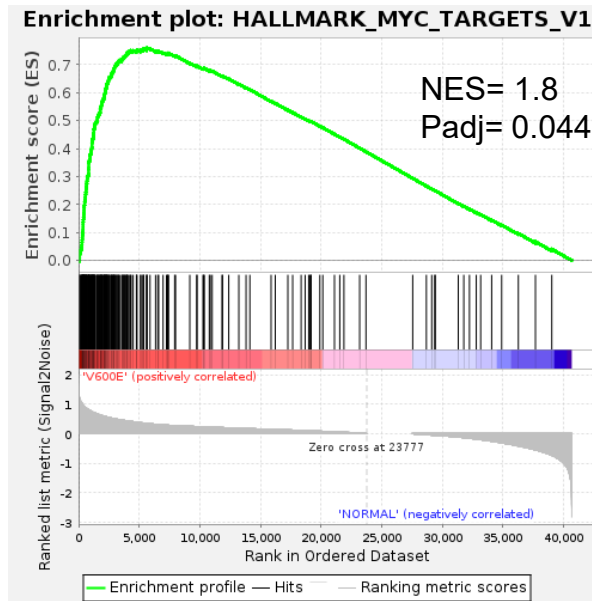
A



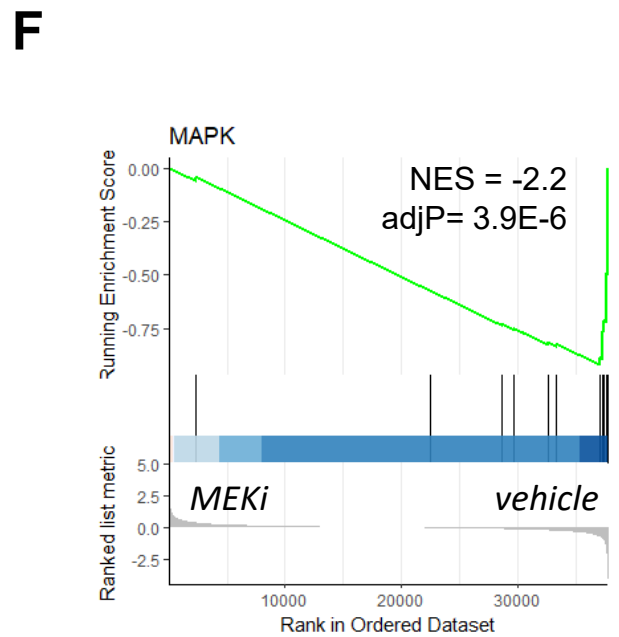
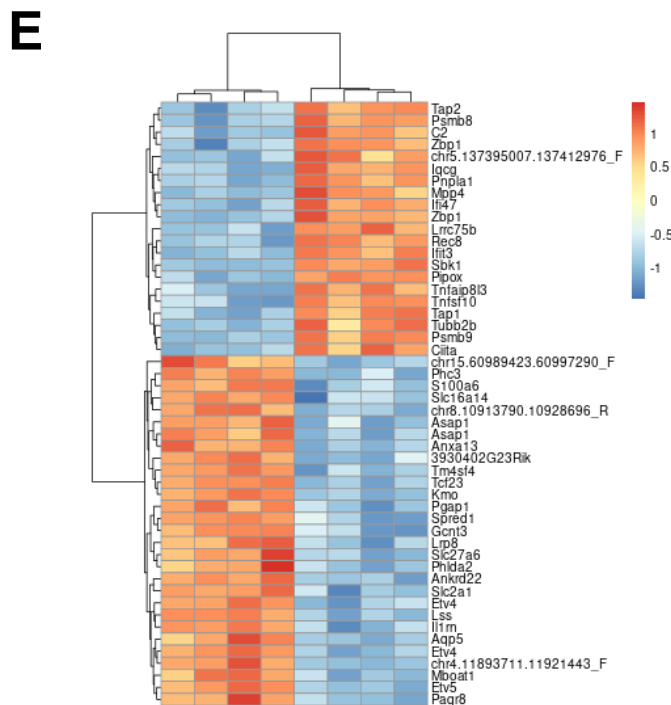
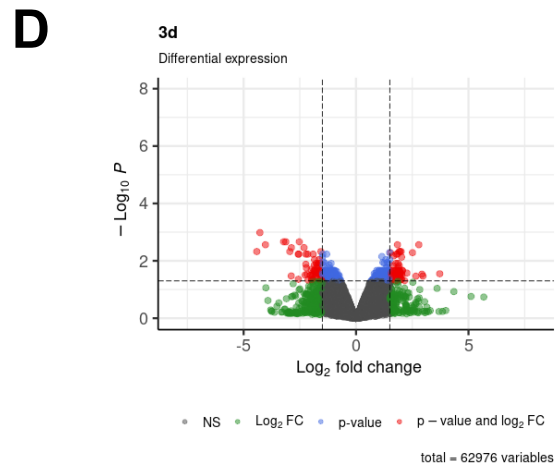
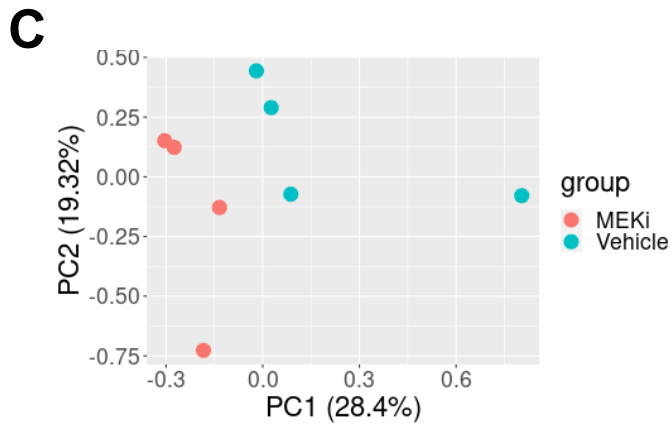
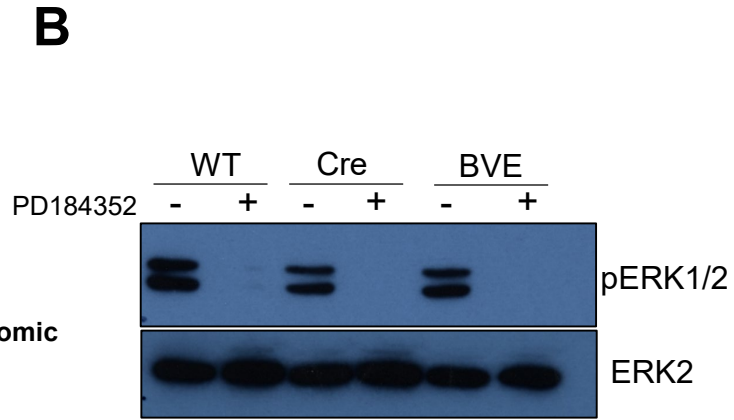
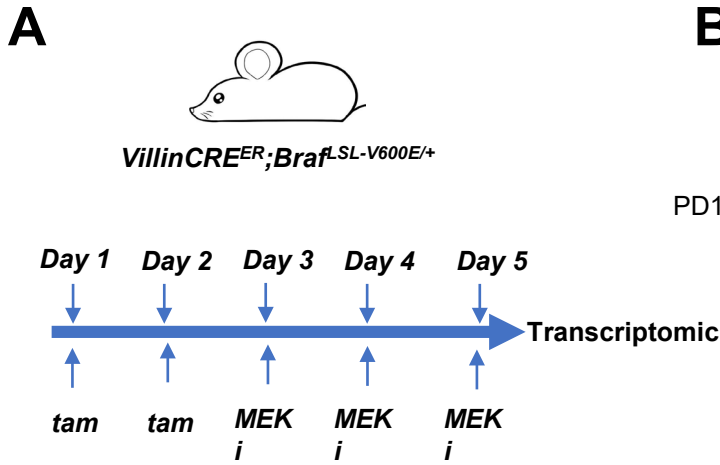
B



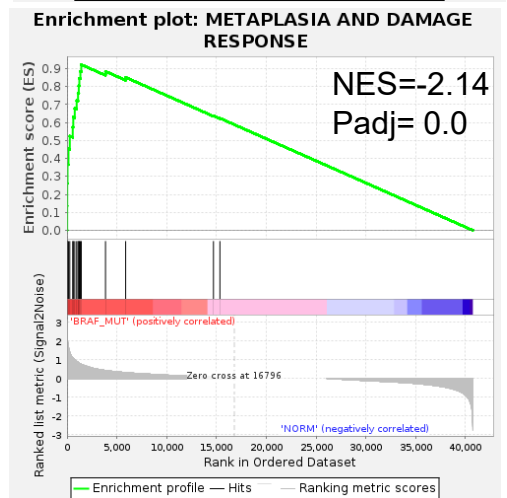
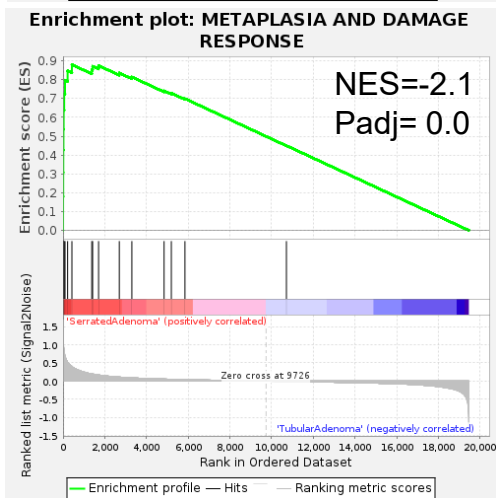
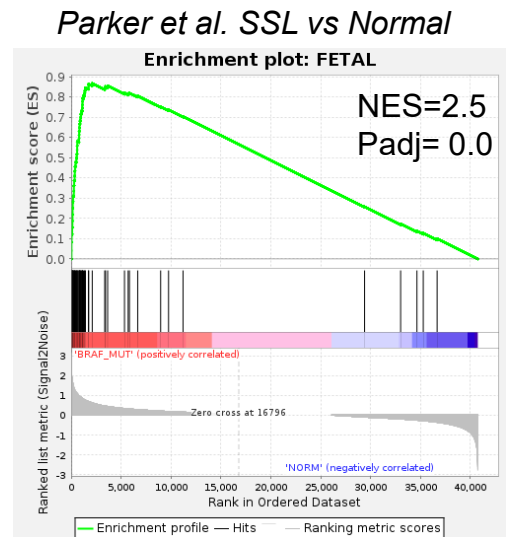
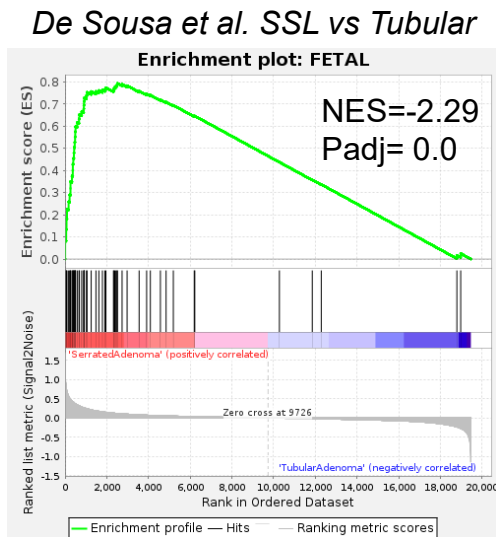
Supplemental Figure 9



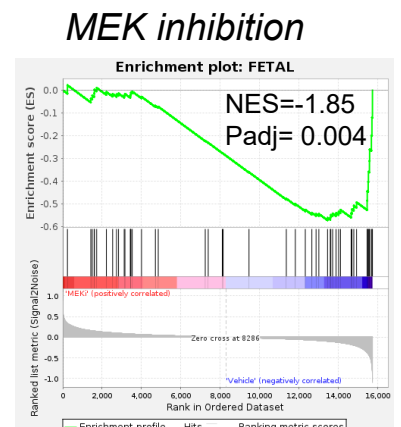
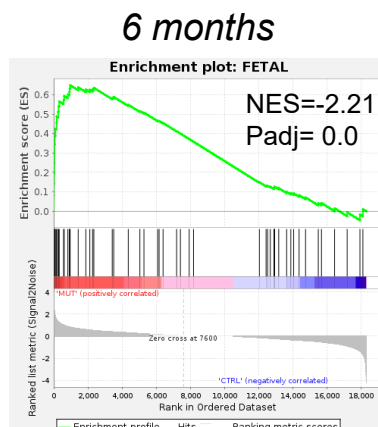
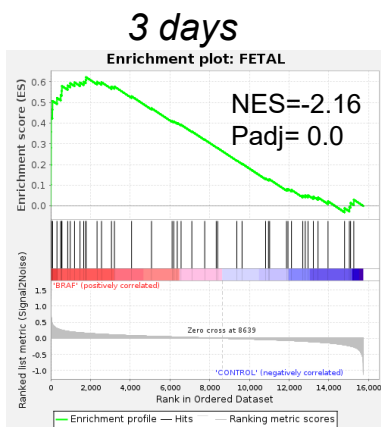
Supplemental Figure 10



A



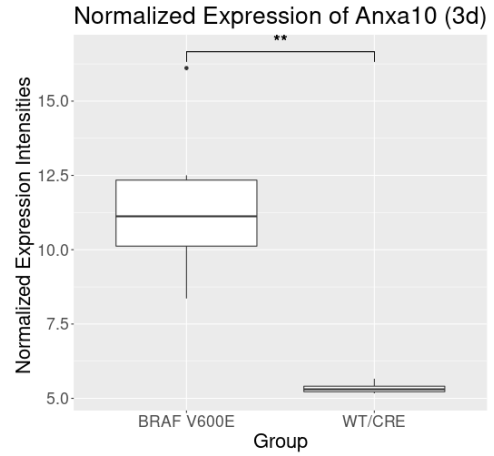
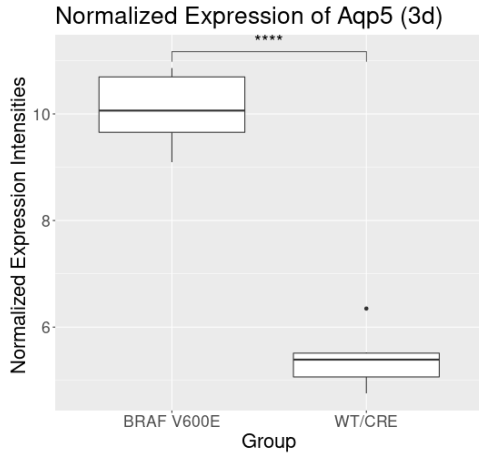
B



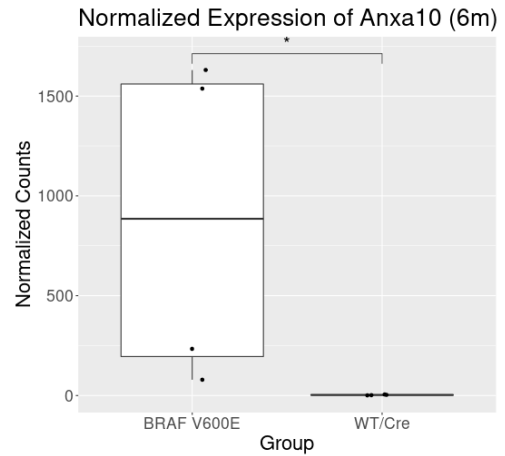
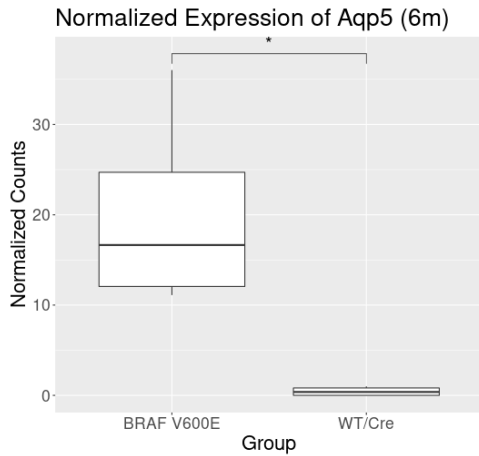
Acquaporin 5

Annexin 10

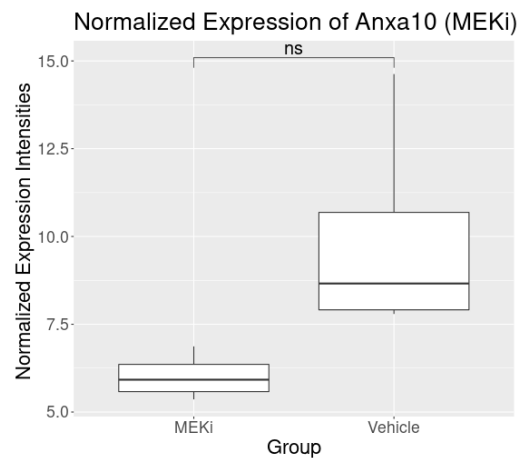
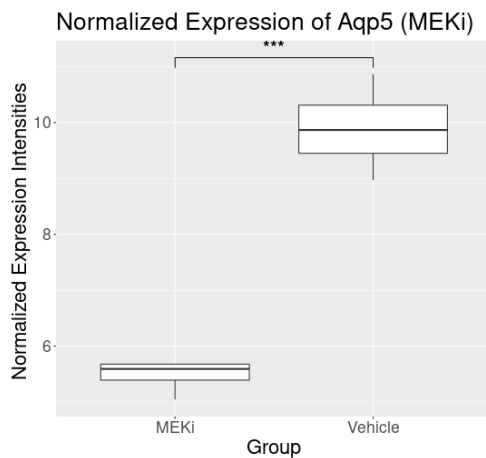
3 days



6 months

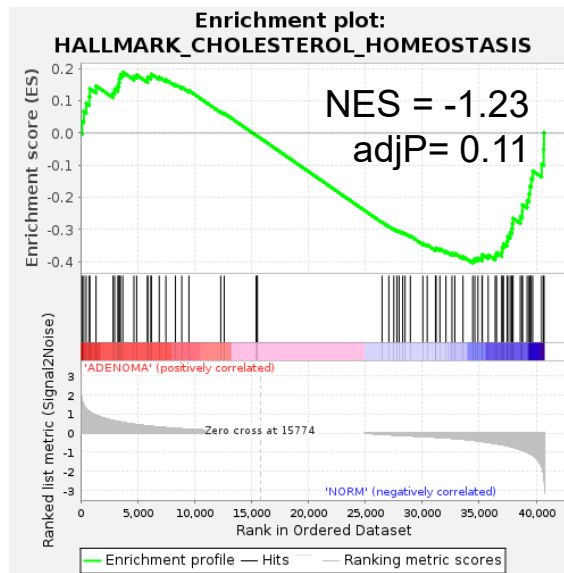


3 days + MEKi

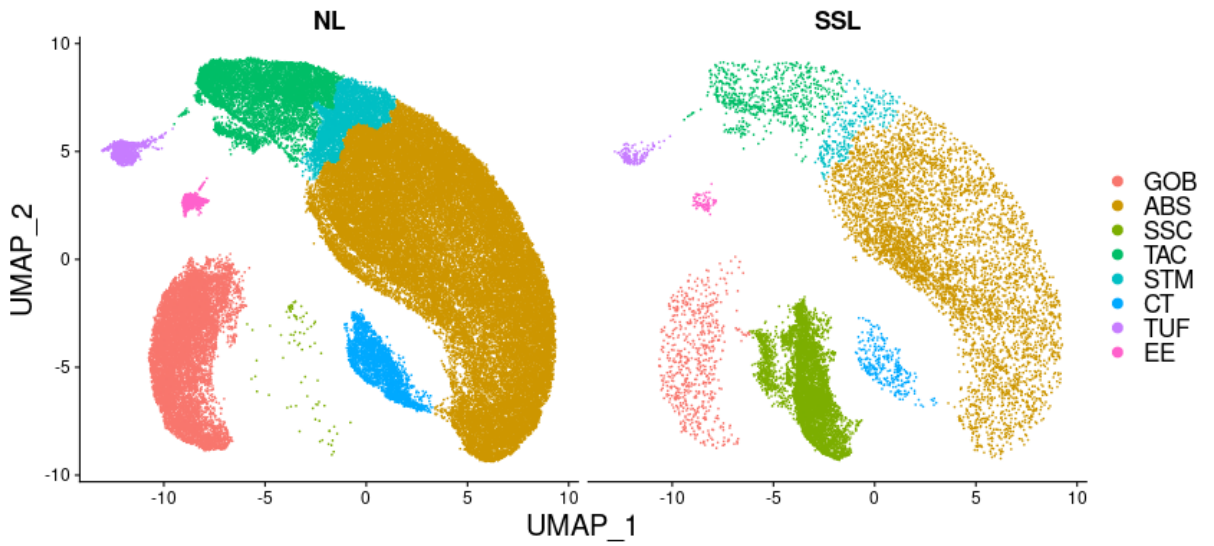


ADs vs normal colon

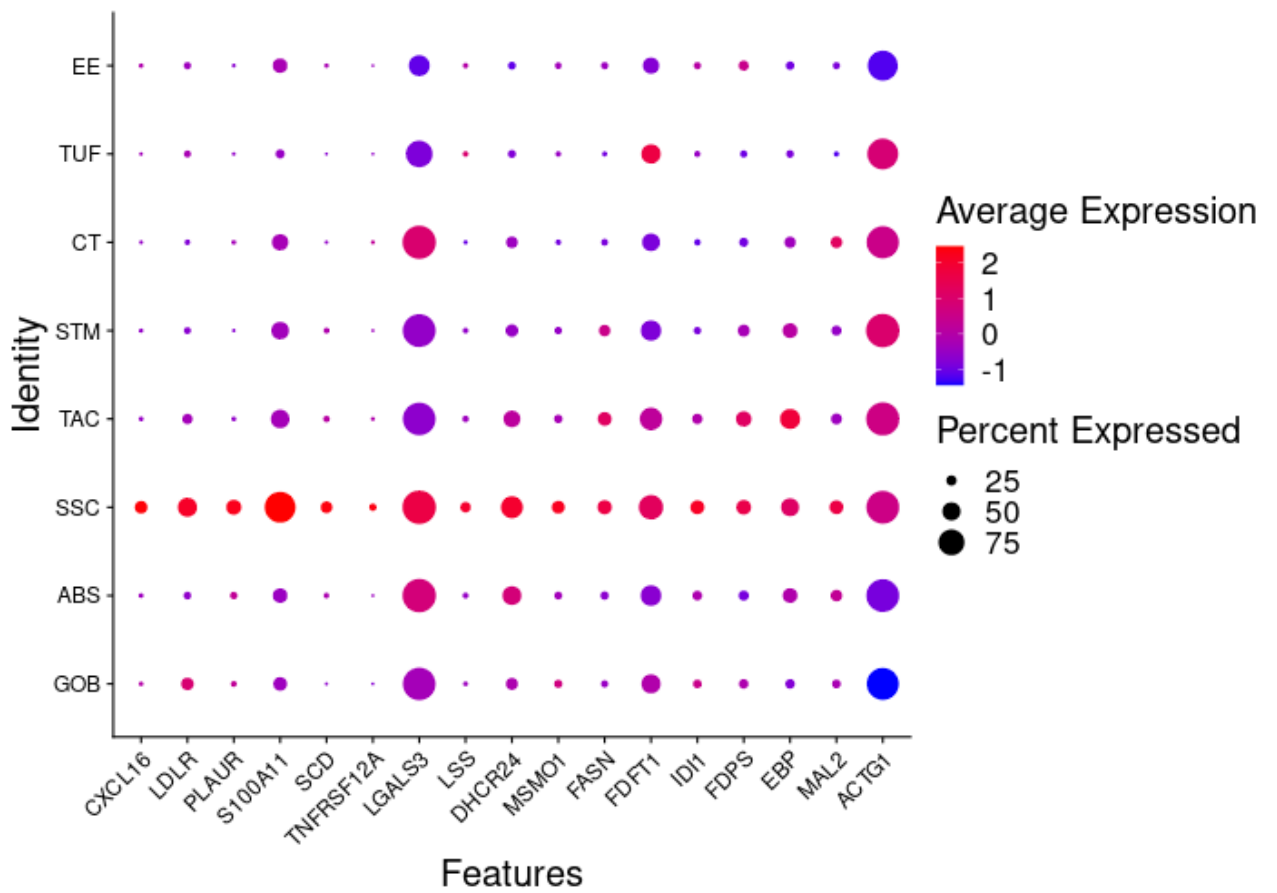
Parker et al.



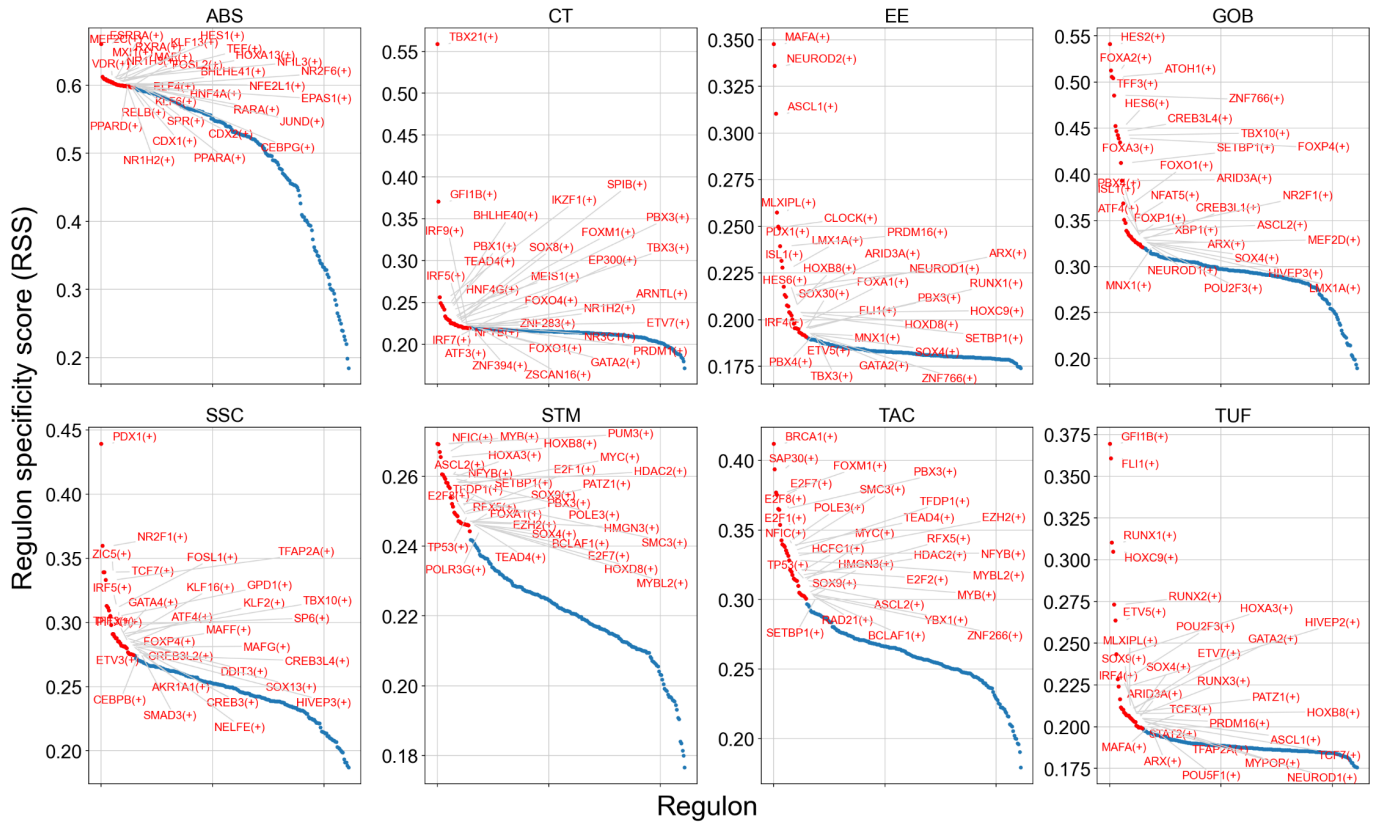
A



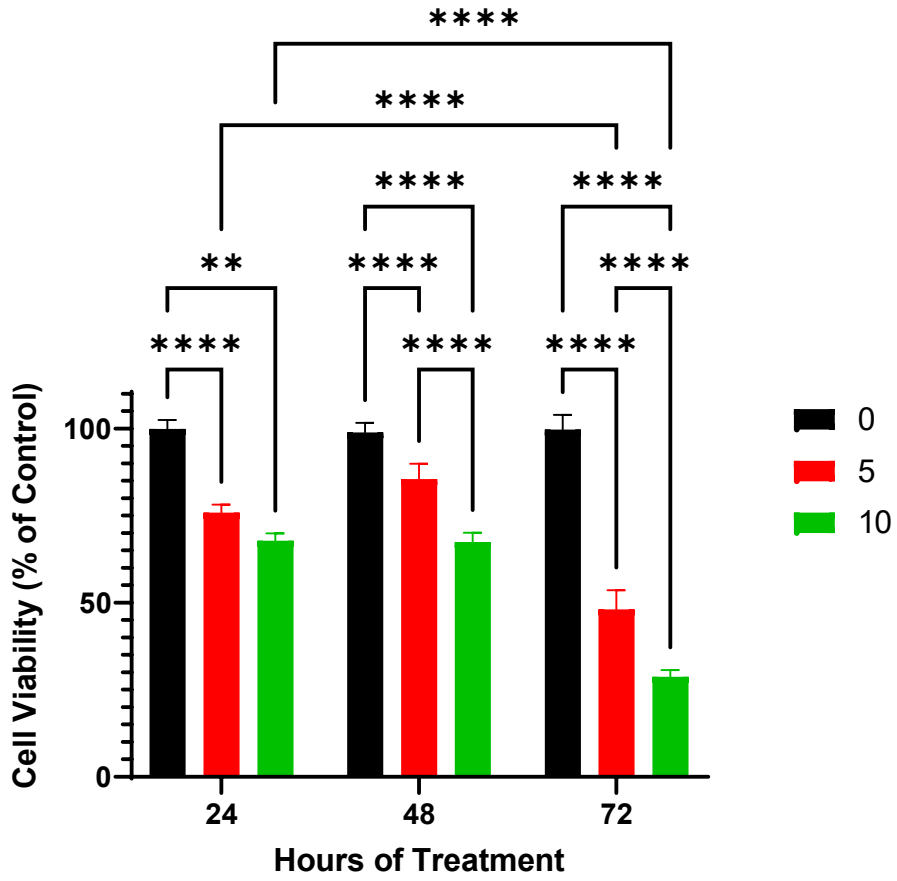
B



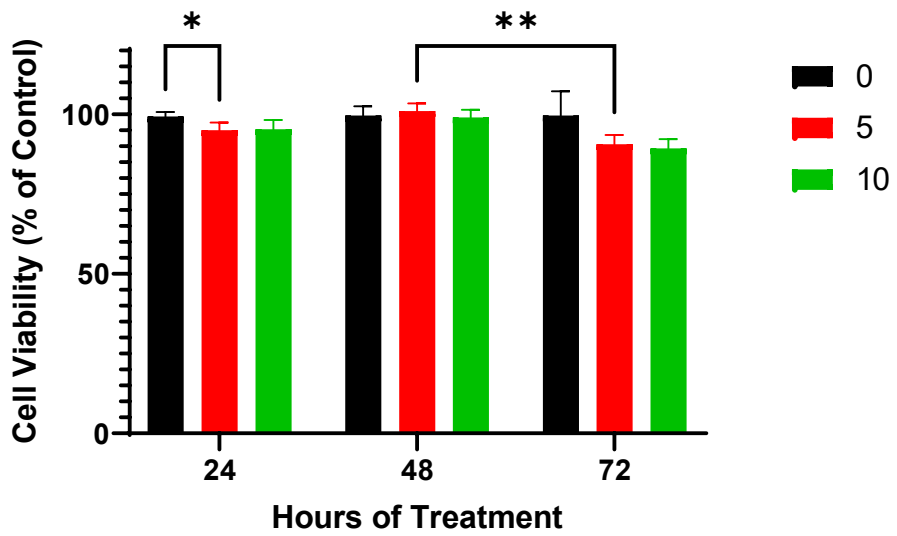
Supplemental Figure 15



A



B



Target	Primers	Sequence
BRAFLSL-V600E/WT	OCP125 (FWD)	5'-GCC-CAG-GCT-CTT-TAT-GAG-AA-3'
	OCP137 (REV-HET)	5'-GCT-TGG-CTG-GAC-GTA-AAC-TC-3'
	OCP 143 (REV-WT)	5'-AGT-CAA-TCA-TCC-ACA-GAG-ACC-T-3'
Villin-CreER ^T	OCP 361 (FWD)	5'-GCC-TGG-TCT-GGA-CAC-ATG-CC-3'
	OCP362 (REV)	5'-GTG-TCA-GCA-TCC-AAC-AAG-GC-3'

Supplemental Table 1. PCR primers used for genotyping.

Target	Supplier	Catalogue	Species	Dilution	Antigen retrieval
Lysozyme	DAKO	A099	Rabbit	1:10,000	Proteinase K
Olfm4	Cell Signalling	39141	Rabbit	1:300	Sodium citrate
Chromogranin A	Immunostar	20085		1:1000	Sodium Citrate
BrdU	Cell Signalling	5292	Mouse	1:200	Sodium Citrate
Cleaved-PARP	Cell Signalling	94885	Rabbit (mono)	1:100	Sodium Citrate

Supplemental Table 2. List of primary antibodies used for IHC and IF.

Name	Fluorophore	Amplicon size (bp)	Assay ID
Lgr5	FAM	64	Mm00438890_m1
Olfm4	FAM	130	Mm01320260_m1
Lyz1	FAM	129	Mm00657323_m1
Alpi	FAM	60	Mm01285814_g1
Muc2	FAM	66	Mm01276696_m1
Chga	FAM	59	Mm00514341_m1
Hmgcr	FAM	64	Mm01282499_m1
Mvk	FAM	67	Mm00445773_m1
Mvd	FAM	109	Mm00507014_m1
Tbp	VIC	65	Mm01277042_m1
Actb	VIC	72	Mm04394036_g1
B2m	VIC	77	Mm00437762_m1
Gusb	VIC	71	Mm01197698_m1

Supplemental Table 3. List of TaqMan assay for rt-qPCR.